STRUCTURAL BASIS OF CALCIUM TRANSPORT AND SELECTIVITY IN THE MITOCHONDRIAL CALCIUM UNIPORTER

APPROVED BY SUPERVISORY COMMITTEE

_____
Youxing Jiang, Ph.D.

_____
Daniel Rosenbaum, Ph.D.

_____
Paul Blount, Ph.D.

_____
Ryan Hibbs, Ph.D.

I proudly dedicate this work to my mom for inspiring me to be the best person that I can be; for her unconditional love; and for supporting me in all of my academic and personal endeavors. The strength and resilience that you have demonstrated throughout your life continue to inspire me to never choose to settle for the path of least resistance.

To John Avila, Jr. for his companionship and constant encouragement on this long journey. You were there to lift me up during the lowest points in my career and I am so happy to share this accomplishment with you.

To Xiaochen Bai for helping me cross the finish line. There are no words for me to express how grateful I am to your contribution to my research.

To my mentor Youxing Jiang for his incredible mentorship and support during my time as a graduate student in his lab. Thank you for giving me the intellectual freedom to grow from a technician into scientist.

STRUCTURAL BASIS OF CALCIUM TRANSPORT AND SELECTIVITY IN THE MITOCHONDRIAL CALCIUM UNIPORTER

by

Nam X. Nguyen

DISSERTATION

Presented to the Faculty of the Graduate School of Biomedical Sciences

The University of Texas Southwestern Medical Center at Dallas

In Partial Fulfillment of the Requirements

For the Degree of

DOCTOR OF PHILOSOPHY

The University of Texas Southwestern Medical Center at Dallas

Dallas, Texas

May, 2018

STRUCTURAL BASIS OF CALCIUM TRANSPORT AND SELECTIVITY IN THE MITOCHONDRIAL CALCIUM UNIPORTER

Nam X. Nguyen, Ph.D.

The University of Texas Southwestern Medical Center at Dallas, 2018

Youxing Jiang, Ph.D.

The mitochondrial calcium uniporter is a highly selective calcium channel localized to the inner mitochondrial membrane. Here, I describe the structure of an MCU ortholog from the fungus *Neosartorya fischerii* (NfMCU) determined to 3.8 Å resolution by phase-plate cryo-electron microscopy. The channel is a homotetramer with two-fold symmetry in its amino terminal domain (NTD) that adopts a similar structure to that of human MCU. The NTD assembles as a dimer of dimer to form a tetrameric ring that connects to the transmembrane domain through an elongated coiled-coil domain. The ion conducting pore domain maintains four-fold symmetry with the selectivity filter positioned at the start of the pore forming TM2 helix. The aspartate and glutamate sidechains of the conserved

DIME motif are oriented toward the central axis and separated by one helical turn. Thus, the structure of NfMCU offers new insights into channel assembly, selective calcium permeation, and inhibitor binding.

Table of Contents

Prior Publications

Nguyen, Y.*, **Nguyen, N.X.***, Rogers, J.L., Liao, J., MacMillan, J.B., Jiang, Y., Sperandio, V. 2015. Structural and mechanistic roles of novel chemical ligands on the SdiA quorum-sensing transcription regulator. *MBio* 6(2):e02429-14. doi:10.1128/mBio.02429-14. (* co-first authors)

Mo, X., **Nguyen, N.X.**, Luo, S.Z., Fan, H., Andrews, R.A., Berndt, M.C., Li, R. 2010. Trans-membrane and trans-subunit regulation of ectodomain shedding of platelet glycoprotein Ibα. *J Biol Chem.* 285(42):32096-104.

Mo, X., **Nguyen, N.X.**, McEwan, P.A., Zheng, X., Lopez, J.A., Emsley, J., Li, R. 2009. Binding of platelet glycoprotein Ibβ through the convex surface of leucine-rich repeats domain of glycoprotein IX. *J Thromb Haemost*. 7(9):1533-40.

List of Figures

List of Tables

List of Abbreviations

ATP	Adenosine triphosphate
$[Ca^{2+}]_{o/i/c/mt}$	Calcium concentration (o: extracellular, i: intracellular, c: cytosoli, mt: mitochondrial
CCD	Coiled-coil domain
CTD	Carboxy-terminal domain
ELISA	Enzyme-linked immunosorbent assay
EMRE	Essential MCU regulator
ER/SR	Endo-/sarcoplasmic reticulum
ETC	Electron transport chain
IP3R	Inositol-1,4,5-triphosphate receptor
MCU	Mitochondrial calcium uniporter
MICU1/2/3	Mitochondrial calcium uptake 1/2/3
MFN2	Mitofusin2
NADH	Nicotinamide adenine dinucleotide
NTD	Amino-terminal domain
P_i	Inorganic phosphate
PTP	Permeability transition pore
ROS	Reactive oxygen species
RyR	Ryanodine receptor
SAD	Single wavelength anomalous diffraction
SEC	Size exclusion chromatography
SMAC	Second mitochondria-derived activator of caspase

TCA	Tricarboxylic acid cycle
TMD	Transmembrane domain

Chapter 1. Introduction

Calcium is a versatile signaling molecule that regulates numerous cellular processes, ranging from metabolism to cell proliferation and apoptosis. Due to the diverse physiological responses triggered by calcium, it is no surprise that cells have evolved an array of mechanisms to decode calcium signaling. One such feature is to maintain a constitutively low cytosolic calcium concentration ($[Ca^{2+}]_{c)}$, thus ensuring that no calcium signaling will occur until the proper signal is present. As such, the resting $[Ca^{2+}]_c$ is roughly 100nM while the extracellular calcium concentration ($[Ca^{2+}]_o$) and those stored within intracellular pools ($[Ca^{2+}]_i$) such as the endoplasmic reticulum (ER) are ~1mM and ~100μM, respectively (Rizzuto, 2012).

The strategic positioning of organelles known to regulate calcium uptake and storage within the cytosol also plays an important role in affecting how a cell responds to calcium. The two most important players in this process are the ER and mitochondria. As the primary site of cellular calcium storage, the ER plays a crucial role in calcium release – via ryanodine receptors (RyR) and inositol-1,4,5-triphosphate receptors (IP3R) – and uptake – via the sarcoendoplasmic reticulum calcium ATPase (SERCA). Mitochondria, on the other hand, function as temporary sites of calcium storage by buffering local increases in cytosolic calcium concentration. The intertwining relationship between the ER and mitochondria was first recognized with the observation that these organelles form close contacts to one another in cells (Rizzuto, 1998), which is essential to the calcium buffering capacity of mitochondria. While calcium released from the ER typically raises the total cytosolic calcium concentration from ~100nM to ~400nM, the calcium concentration near IP3Rs are significantly higher. The activation of IP3Rs produce

microdomains of cytosolic Ca^{2+} concentrations in the low micromolar range, which stimulates rapid mitochondrial calcium uptake (Rizzuto, 1993). Efficient calcium uptake by mitochondria at these microdomains requires the membranes of the ER and mitochondria to maintain a close distance to one another, which is mediated by the tethering protein mitofusin2 (MFN2), a mitochondrial dynamin-related GTPase (de Brito, 2008). ER localized MFN2 forms both homo- and heterotypic interactions with mitochondrial localized MFN1 or 2, allowing for inter-organellar communications to occur. Disruption of their interactions in cells increases the distance between the ER and mitochondria, changes ER and mitochondria morphology, and reduces mitochondrial calcium uptake. Further highlighting the importance of the ER-mitochondria interaction are *in vivo* experiments showing that *Mfn2* knockout in mice is embryonic lethal and mutations in Mfn2 in humans cause Charcot-Marie-Tooth type IIa neuropathy (Züchner, 2004). In addition to MFN2, it has also been reported that IP3R and the non-selective, voltage-dependent anion channel (VDAC, localized to the outer mitochondrial membrane) interact through a chaperone called glucose-regulated protein 75 (Szabadkai, 2006). Thus, the spatiotemporal regulation of calcium signaling through the positioning of mitochondria near calcium release sites on the ER membrane is an important regulatory mechanism for calcium homeostasis.

Another way that cells have evolved to decode calcium signaling is through the broad range of molecules that detect and respond to calcium itself. Central to the maintenance of a cell's calcium concentration gradient are ion channels and transporters that selectively move Ca^{2+} across biological membranes, which can elevate or deplete the cytosolic calcium concentration ($[Ca^{2+}]_c$). IP3R, for example, which functions as the

primary intracellular calcium release valve, is known to be regulated by $[Ca^{2+}]_c$, with the channel open probability increasing as cytosolic Ca^{2+} increases from 0 to 0.25μM and then becoming inhibited at higher calcium concentrations (Bezprozvanny, 1991). The mitochondria calcium uniporter (MCU), which is the primary calcium uptake machinery in mitochondria and will be discussed subsequently in greater detail, requires $[Ca^{2+}]$ greater than 500nM to become activated (Gunter, 1990). Thus, like the ER and mitochondria, the strategic positioning of calcium sensing and transporting proteins within a cell can both fine tune and effect cellular responses. In *Xenopus* oocytes, for example, the propagation of calcium waves depends on the interplay between IP3R and MCU (Jouaville, 1995). Simply changing the energetic state of mitochondria, which affects the mitochondrial proton gradient and, ultimately, the driving force for MCU, can dramatically change the frequency and amplitude of the calcium waves produced by IP3Rs. One physiological consequence of a change in calcium dynamics is the effect that Ca^{2+} has on gene regulation and cell development. T-cells, for example, utilize the frequency of intracellular calcium oscillations to activate specific pro-inflammatory transcription factors (Dolmetsch, 1998). While gene regulation utilizes calcium oscillations that can last for many minutes, other processes such as vesicle fusion require only a transient increase in cytoplasmic calcium concentration, lasting only several milliseconds (Berridge, 2003). Thus, calcium concentration fluctuations can be decoded within a cell across several timescales.

Mitochondria and calcium signaling

While mitochondria are typically defined as the powerhouses of a cell due their role in ATP production, they have long been known to play an important role in calcium signaling. The relationship between calcium and mitochondria was initially discovered with the serendipitous observation that mitochondria buffered calcium, which occurred at the same time that the chemiosmotic hypothesis was being elucidated. The decades following this discovery have revealed an unambiguous role between calcium and this ancient organelle.

For instance, mitochondrial calcium uptake affects metabolism by regulating mitochondrial matrix enzymes within the tricarboxylic acid (TCA) cycle, namely pyruvate dehydrogenase, isocitrate dehydrogenase, and α-ketoglutarate dehydrogenase (Rizzuto, 2012). Activation of TCA dehydrogenases increases the production of NADH, which functions as the energy currency used by the electron transport chain (ETC) for the production of ATP under aerobic conditions. As NADH is fed into the ETC, the energy stored in NADH is used to pump H^+ from the mitochondrial matrix into the intermembrane space, producing the proton gradient, thus giving rise to the mitochondrial membrane potential. The proton gradient is then used by the F_1F_o ATPase to drive the production of ATP. Thus, an elevated $[Ca^{2+}]_c$ would increase $[Ca^{2+}]_{mt}$ and directly affect cellular energy homeostasis.

Due to their role in oxidative phosphorylation, mitochondria are also important sites of redox chemistry. As NADH molecules enter the ETC, they become oxidized and pass their electrons to carriers within complex I, II, and III of the ETC. The electrons must then

be passed on to oxygen in order for the electron carriers to become available recipients of additional electrons from other NADH molecules; absent of oxygen (i.e. under anaerobic conditions), the ETC becomes stalled. However, reduction of oxygen produces reactive superoxide anions, which can react with proteins and nucleic acids within the mitochondria, leading to cellular damage. Typically, superoxide anions are converted to the more stable peroxide (H_2O_2) by the mitochondrial matrix enzyme Mn superoxide dismutase or the mitochondrial intermembrane space and cytosolic Cu/Zn superoxide dismutase. H_2O_2 is then converted to water by mitochondrial and cytosolic glutathione peroxidase or by peroxisomal catalase. However, elevated levels of H_2O_2 can react with transition metals to produce hydroxyl radicals, which can lead to cellular oxidative damage by targeting iron-sulfur centers of mitochondrial enzymes (Wallace, 2005). The cumulative effect of cellular damage from oxygen radicals is ultimately cell death.

While cell death is a tightly regulated process, a potent activator of apoptosis is a prolonged elevation in mitochondrial calcium concentration (Clapham, 2007). Mitochondrial calcium overload triggers the opening of the permeability transition pore (PTP), a channel-like protein that spans the inner and outer mitochondrial membrane. Opening of the PTP uncouples the mitochondrial membrane potential and allows for the release of mitochondrial matrix contents such as cytochrome c and second mitochondria-derived activator of caspase (SMAC) into the cytosol. Cytochrome c then binds to APAF1 in the cytosol to form the apoptosome, which is followed by the recruitment of pro-caspase 9 to the apoptosome and its activation. SMAC further promotes apoptosis by binding to inhibitors of apoptosis proteins in the cytosol, which allows for the activation of pro-

caspase 9. Thus, mitochondrial calcium homeostasis plays a pivotal role in the life and death of a cell.

History of mitochondrial calcium uptake

Mitochondrial calcium transport was initially discovered in the early 1960s with the observation that mitochondria isolated from rat kidney take up large amounts of calcium from their environment (DeLuca, 1961, Vasington, 1962). However, studies on mitochondrial ion transport began in the early 1950s, which showed that energized mitochondria can accumulate K^+ and Mg^{2+}. However, as the field was trying to arrive at a mechanistic understanding of how mitochondria produced ATP, interest grew in the area of mitochondrial ion transport because of the hypothesis that ion movement across the mitochondrial membrane could provide the driving force for ATP synthesis (Lehninger, 1967).

The years following the initial observation of mitochondrial calcium uptake were aimed at defining the basic properties as well as developing a mechanistic understanding of the process. First, inorganic phosphate (P_i) is required for “massive loading” of Ca^{2+} in mitochondria, which is characterized by the rapid uptake and retention of Ca^{2+} from the medium over time. In the absence of P_i, calcium uptake proceeds at a significantly slower rate and the Ca^{2+} entering the mitochondria would gradually extrude from the matrix into the reaction medium (Bygrave, 1977). Thus, P_i functions to sequester Ca^{2+} in the mitochondrial matrix.

Additionally, calcium uptake depends on the mitochondrial proton gradient, which sets up a mitochondrial membrane potential of approximately -180mV and is maintained by the translocation of proton from the mitochondrial matrix to the intermembrane space through the oxidation of respiratory intermediates (Gunter, 1990). Although early studies on purified mitochondria showed that the presence of Mg^{2+}, ATP, and an oxidizable respiratory substrate in the reaction medium were required to mediate massive calcium loading, the underlying mechanism was unclear (Vasington, 1962). Ultimately, attempts to probe the underlying mechanism for calcium uptake all pointed toward the mitochondrial proton gradient. First, it was shown that disrupting the mitochondrial membrane potential through the use of uncouplers like the proton ionophore, 2,4-dinitrophenol, abolished calcium uptake (Carafoli, 1971). Second, when a respiratory substrate is in the reaction, calcium uptake occurs in the presence of oligomycin – a V-ATPase (or vacuolar type ATPase) inhibitor – but not in the presence of rotenone or other electron transport chain inhibitors; in the absence of a respiratory substrate, ATP is required for calcium uptake and is abolished when oligomycin is added to the reaction (Lehninger, 1967). These findings thus highlight a clear mechanism. The presence of a respiratory substrate allows mitochondria to carry out oxidative phosphorylation, which drives the movement of protons from the matrix to the intermembrane space as electrons are shuttled along the electron transport chain, thus generating an electrochemical gradient that favors calcium uptake. In the absence of an oxidizable respiratory substrate, mitochondria can also produce a proton gradient by running the oxidative phosphorylation reaction in reverse – hydrolyzing ATP and pumping proton into the intermembrane space against its chemical gradient. Thus, the effects of oligomycin, which blocks the F_o subunit

of the F_1F_o ATPase, is only manifested in the absence of a respiratory substrate. Interestingly, calcium uptake can also be driven by the addition of the K^+ selective ionophore, valinomycin, to purified mitochondria, further highlighting the importance of the mitochondrial membrane potential for calcium transport (Scarpa, 1970). Collectively, these observations also led to the assignment of the molecular identity responsible for calcium uptake as the “mitochondrial calcium uniporter” or MCU since calcium uptake proceeded in only one direction (into the mitochondrial matrix) and at a much greater rate than known transporters (Gunter, 1990).

The MCU also exhibits unique ion and inhibitor binding properties. It binds divalent cations in the order of $Ca^{2+} > Sr^{2+} >> Mn^{2+} > Ba^{2+}$ as well as lanthanides; it is blocked by nanomolar concentrations of the inhibitor ruthenium red (Gunter, 1990). Although ruthenium red blocked the MCU, it is a nonspecific inhibitor that is capable of blocking a plethora of other channels and transporters including ryanodine receptors, IP3 receptors, L-type calcium channels, and Na^+/Ca^{2+} exchangers. While ruthenium red became a pharmacological signature of the MCU, its nonspecificity also limited its use in the molecular identification of the MCU. Eventually, Ru360, a compound purified from ruthenium red, was identified as the MCU specific inhibitor (Ying, 1991, Matlib, 1998).

Since the discovery of mitochondrial calcium uptake in the early 1960s, efforts to define the properties of MCU relied on measuring calcium uptake by mitochondria in suspension. While the patch clamp technique is the method of choice for studying ion channels, its application to the study of MCU was limited by the technical challenge of patch clamping mitochondria. Because MCU is localized to the inner mitochondrial membrane, electrical recordings of MCU currents require, first, the removal of the outer

mitochondrial membrane. This can be accomplished by hypotonic treatment of isolated mitochondria to produce inner mitochondrial membrane vesicles called mitoplasts, which typically measure only 2 – 5μm in diameter. In a landmark paper in 2004, David Clapham's lab published the first electrical recordings of MCU by patch clamping mitoplasts isolated from COS-7 cells (Kirichok, 2004). The MCU current or I_{MiCa} is highly selective for Ca^{2+}, with a $K_D \leq 2nM$. Although MCU conducts Na^+, 100nM Ca^{2+} completely inhibits the sodium current, suggesting that at physiological conditions, MCU is impermeable to monovalent cations. These recordings also confirm results from earlier studies: the selectivity of MCU and its inhibition by RuRed and Ru360, with an IC_{50} of 9nM and 2nM, respectively. Single channel recordings of MCU show that the channel exhibits multiple subconductance states measuring between 2.6 – 5.2 pS, which is significantly smaller than that of classical voltage-gated ion channels. Voltage-gated sodium and calcium channels exhibit single channel conductance in the range of 16 – 30pS while some voltage-gated potassium channels (such as BK channels) can exhibit single channel conductance near 300pS (Hille, 2001).

The molecular era of the mitochondrial calcium uniporter

Molecular identification of the mitochondrial calcium uniporter (MCU) evaded the field for many decades until 2010 when the Mootha lab identified the first component of the MCU – a 54kD protein called MICU1 or mitochondrial calcium uptake 1 (Perocchi, 2010). MICU1 is a calcium binding protein containing a pair of EF-hands flanking a pair of pseudo-EF hands (due to the absence of calcium coordinating residues) and is

localized to the intermembrane space of the mitochondria. MICU1 functions as a gatekeeper of the MCU, preventing mitochondrial calcium overload and resulting stresses such as reactive oxygen species (ROS) production and apoptotic stress (Mallilankaraman, 2012). Among metazoans, MICU1 contains two additional paralogs – MICU2 and MICU3 – that heterodimerize with MICU1 to fine tune MCU's sensitivity to cytosolic calcium concentration (Kamer, 2014, Patron, 2014, Plovanich, 2013). Distribution of these MICU paralogs are tissue specific with MICU3 being highly enriched in neuronal tissues.

In 2011, the Mootha lab and the Rizzuto lab simultaneously identified the gene *ccdc109a* as the channel component or MCU of the mitochondrial calcium uniporter (Baughman, 2011, De Stefani, 2011). MCU is a ~35kD protein with two transmembrane (TM) helices flanked by a large amino-terminal domain (NTD) and a short carboxy-terminal domain (CTD); a highly conserved stretch of residues called the DIME motif forms the selectivity filter of the channel (Fig. 1A and 2B). Mutation to the acidic residues of the DIME motif abolishes calcium uptake; additionally, a serine that is located two residues upstream of the DIME motif has been shown to be important for ruthenium red and Ru360 binding, all of which supports the identity of CCDC109A as the uniporter (Baughman, 2011). Like MICU1, metazoan MCU has a paralog called MCUb that is encoded by the gene *ccdc109b* (Raffaello, 2013). However, unlike MCU, homo-oligomers of MCUb are non-functional and, in native tissues, MCUb hetero-oligomerizes with MCU and functions as a negative regulator of the channel (Fig. 1A, B). Furthermore, MCUb's distribution in mouse is tissue specific – enriched in the lung, heart and brain. How MCUb functions *in vivo* and how it modulates channel activity remain unclear.

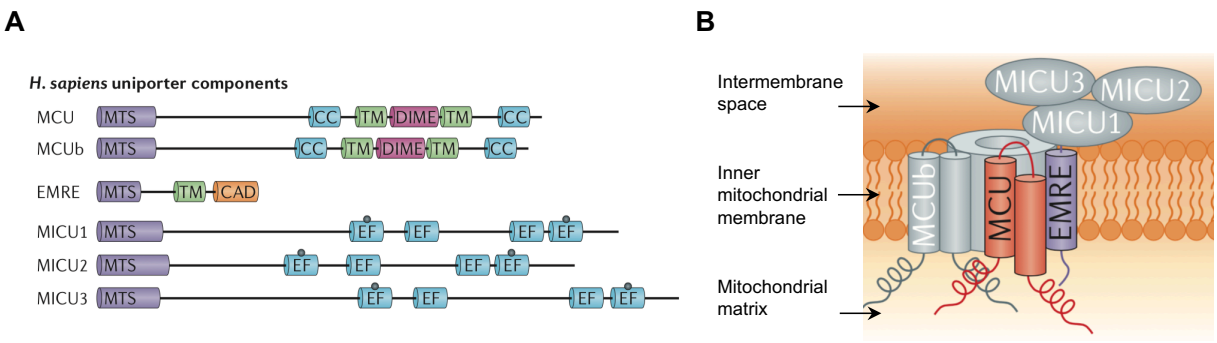

Figure 1. Components of the human mitochondrial calcium uniporter. A, Components of the human MCU complex are shown with specific domains indicated: MTS (mitochondrial targeting sequence, CC (coiled-coil domain), TM (transmembrane domain), DIME (selectivity filter sequence), CAD (C-terminal acidic domain), EF (EF hand domain). **B**, Schematic of the human MCU complex. The ion conducting pore consists of hetero-oligomers of MCU and MCUb. The metazoan-specific EMRE protein binds to MCU to activate the channel. The gate-keeping MICU proteins form hetero-oligomers in the intermembrane space and binds to MCU through EMRE to inhibit the channel. (Note: This figure was reproduced from (Kamer, 2015).)

In 2013, the Mootha lab identified a third crucial component of the mitochondrial calcium uniporter, a ~10kD, single TM spanning protein with a highly conserved carboxy-terminal tail that is rich in acidic residues called EMRE or essential MCU regulator (Fig. 1A, B) (Sancak, 2013). Calcium uptake measurements in a number of different cell lines and electrophysiology recording on whole mitoplasts show that EMRE is required for MCU's function (Sancak, 2013). Additionally, *in vitro* reconstitution of MCU in Baker's yeast, whose genome does not encode for any MCU component, also recapitulates observations made in mammalian cell lines (Kovacs-Bogdan, 2014). The relevance of EMRE, however, has been called into question by electrophysiology recordings done by the Rizzuto lab, which shows that heterologously expressed human MCU alone, when reconstituted into lipid bilayers, is capable of conducting Ca^{2+} (De Stefani, 2011, Raffaello, 2013, Patron, 2014). While these conflicting results have led to confusion in the field, it is worth noting that the channel properties reported in the studies by the Rizzuto lab do not resemble channel properties of the MCU originally characterized through direct patch-clamp recordings on whole mitoplast (Kirichok, 2004). Currently, it seems as though the field has come to a consensus that EMRE is indeed required for the function of MCU (Tsai, 2016, Wu, 2018).

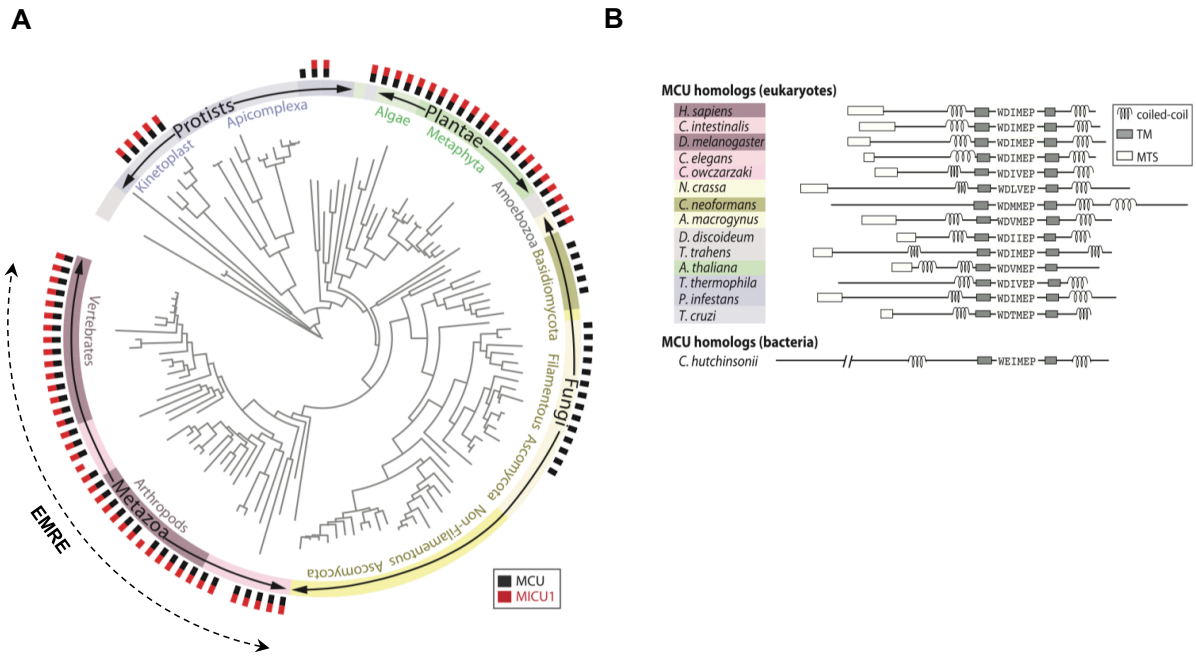

Figure 2. Evolutionary conservation of the mitochondrial calcium uniporter. A, Phylogenetic tree showing the distribution of MCU and MICU1 across eukaryotic taxa. The single transmembrane spanning protein EMRE is found only among metazoans. **B**, Structural conservation of MCU among representative eukaryotic taxa. The region spanning the two coiled-coil domains are most conserved among MCU orthologs. The selectivity filter or DIME motif is indicated by single letter amino acid sequence. (Note: This figure was reproduced from (Bick, 2012).)

Thus, in humans, the mitochondrial calcium uniporter or uniplex is a protein complex consisting of at least four components: the ion conducting pore – MCU, an essential membrane spanning subunit – EMRE, and peripheral membrane gate-keeping proteins – MICU1 and MICU2 (Fig. 1A). The current molecular model of the uniplex is as follows: MCU forms the calcium conducting channel and is gated by MICU1 and MICU2; EMRE interacts with MCU through its TM spanning helix and directly couples MICU1 to the uniplex through its C-terminal acidic tail (Fig. 1B). Interestingly, sequence analysis shows that while MCU is found in all major eukaryotic taxa, EMRE is metazoan specific (Fig. 2A) (Bick, 2012, Sancak, 2013). In fact, the mitochondrial calcium uniporter is evolutionarily diverse. For instance, fungi only encode for the ion conducting subunit of the uniplex while protozoa and plants encode for MCU and the gate-keeping protein MICU1 (Fig. 2A). Unlike metazoan MCU, which requires EMRE to function, fungal and *Dictyostelium* MCU are fully functional (Carafoli, 1971, Kovacs-Bogdan, 2014, Song, 2016). Thus, a fundamental question that arises from this observation is: Why have metazoan MCUs evolved to require EMRE to be functional?

Since the molecular identification of MCU, the field has moved in the direction of arriving at a mechanistic understanding of how the channel functions. Despite this interest, much remains to be discovered and even more conundrums await clarification. For instance, despite its ubiquitous expression in mouse, complete knockout of MCU is not entirely embryonic lethal and nor is mitochondrial calcium accumulation completely abolished (Pan, 2013). In fact, matrix calcium from $MCU^{-/-}$ skeletal muscle mitochondria was only reduced to 25% that of wildtype mitochondria, which suggests an alternative mechanism for mitochondrial calcium uptake *in vivo*. Additionally, when *ccdc109a* (the

gene encoding MCU in mouse) was abolished in the outbred CD1 mouse strain, the resulting $MCU^{-/-}$ mice were viable even though they exhibited reduced size and an inability to perform strenuous exercise as compared to wildtype mice. This result certainly came as a surprise to the field given nearly half a century of work showing the importance of MCU to mitochondrial calcium uptake and the role of calcium in regulating numerous cellular processes. Interestingly, in the genetically pure inbred C57BL/6 mouse strain, MCU knockout resulted in embryonic lethality, with mice dying between E11.5 and E13.5 (Murphy, 2014). The drastically different phenotype between the mouse strains is yet another surprising discovery that lacks a clear explanation. While the $MCU^{-/-}$ CD1 mice are viable, it is worth noting that when $MCU^{+/-}$ CD1 mice are crossed, the resulting offspring are not in the expected Mendelian ratio of 1:2:1. Instead of the expected 25% $MCU^{-/-}$, the authors report only a 12-15% for the cohort, which suggests a significant impact of MCU on embryonic lethality even in the viable CD1 mouse strain (Murphy, 2014).

While the phenotypes from these $MCU^{-/-}$ mouse models have been perplexing, the physiological relevance of MCU is undeniable. Recently, the first human mutations mapped to the uniplex was identified (Logan, 2014): truncating mutations in the MICU1 gene among patients resulted in a complete loss of MICU1 expression. The clinical hallmarks among these patients include skeletal muscle myopathy, encephalopathy, learning disability and movement disorder. Fibroblasts isolated from these patients showed defect in calcium handling and morphological pathology; specifically, the mitochondria network showed severe fragmentation. Recently, these phenotypes were recapitulated in $MICU1^{-/-}$ mice (Liu, 2016b). Interestingly, this study showed that mitochondrial calcium overload can be alleviated by reducing the expression of the

metazoan specific MCU regulator EMRE. First, this observation confirms the functional relevance of EMRE to the metazoan uniplex *in vivo*. Second, rescue of the deleterious phenotypes exhibited by MICU1$^{-/-}$ mice offers a proof of principle for the potential genetic manipulation of the uniplex for the therapeutic intervention of MCU related disorders. Collectively, in the ~50 years that has elapsed since the initial discovery of calcium uptake by rat liver mitochondria, much has been learned about this unexpected phenomenon. However, several fundamental questions still remain: 1) Given MCU's unique primary sequence, what is its overall architecture and how does it compare to other calcium channels? 2) What structural constraints allow MCU to accomplish high affinity calcium binding while mediating rapid calcium uptake? 3) What are the structural differences between those MCUs that conducts calcium in the absence of EMRE and those that require EMRE to function? 4) How does MCU, EMRE, and MICU1 function as a molecular complex?

Chapter 2. Methodology

In this chapter, I describe the approaches used to study the structure and function of MCU. Given the recent identification of the molecular components of the mitochondrial calcium uniporter, structural studies on the channel is rather limited. However, previous structural studies on human MICU1 (Wang, 2014), the amino terminal domain (NTD) of human MCU (Lee, 2015), and the pore domain of *C. elegans* MCU (Oxenoid, 2016) show that various components of the uniporter can be readily expressed in bacteria. Functional studies on MCU are much more abundant in the literature but typically involve measuring calcium uptake from purified mitochondria (Gunter, 1990). Recently, two other approaches have been introduced: mitoplast patch clamp (Kirichok, 2004) and reconstitution in Baker's yeast (Kovacs-Bogdan, 2014). The mitoplast patch clamp technique was developed in David Clapham's lab in 2004 but has seen limited application to the study of MCU due to the technical challenge of patching such a small organelle, which measures only 2-5μm in diameter. Vamsi Mootha's lab recently showed that mitochondria of *S. cerevisiae*, which does not express MCU and, thus, do not exhibit uniporter activity, can mediate calcium uptake when reconstituted with human or *D. discoideum* MCU. Interestingly, reconstitution of *Trypanosome cruzi* MCU did not confer uniporter activity in yeast mitochondria even though the channel mediates calcium uptake in mitochondria of *T. cruzi* (Chiurillo, 2017). Thus, it is not known whether *T. cruzi* MCU requires additional components to form a functional channel or whether yeast mitochondria cannot fully reconstitute uniporter activity for all MCU orthologs.

Although I tested MCU expression in several heterologous expression systems including *E. coli*, *S. cerevisiae*, Sf9 insect cells, and HEK293F cells, MCU can be

expressed to milligram quantity in bacteria and was chosen for further biochemical and structural studies. This observation is in agreement with previously published structural studies on various components of metazoan MCU (Wang, 2014, Lee, 2015, Oxenoid, 2016). To study the function of NfMCU, I exerted a great deal of effort to measure channel activity by patch clamping NfMCU proteoliposomes. However, I could not detect any channel current that satisfied all of the classical properties of the uniporter, namely, high selectivity for Ca^{2+} over Na^{+}, inhibition by RuR and Ru360, and competitive inhibition by Gd^{3+} (Gunter, 1990). Thus, I developed two assays for studying the function of NfMCU: bacteria calcium uptake assay and a $^{45}Ca^{2+}$ flux assay. The bacteria calcium uptake assay would function as a readout for properly folded channel that are localized to the plasma membrane of the host *E. coli*. Additionally, the membrane potential across the inner bacterial membrane is quite similar to that of mitochondria, measuring approximately -140mV in bacteria (Lo, 2007) as compared to -180mV across the inner mitochondrial membrane (Gunter, 1990). In the radioactive calcium flux assay, I seek to validate the functional integrity of the purified channel following extraction from the host membrane and purification in detergent. Finally, I describe in this section several noteworthy technical tools that have only been recently introduced for the structural study of membrane proteins: reconstitution of membrane proteins into artificial lipids stabilized by the scaffold protein saposin A and cryo-EM data collection using a Volta phase plate to improve protein contrast in vitreous ice. I predict that the nuanced modifications I made to the protocol for the reconstitution of membrane proteins into artificial lipid bilayers will be particularly useful for future studies on those proteins that are unstable or sensitive to harsh biochemical treatments.

Protein expression and purification

I initially screened 25 MCU orthologs, which represents all the major eukaryotic taxa known to encode MCU to identify constructs that are suitable for structural studies. The constructs (a generous gift from Dr. Vamsi Mootha, HHMI, Massachusetts General Hospital), which were codon optimized for expression in *E. coli* and had their mitochondrial targeting sequence removed, were cloned into the pCOLD II expression vector using restriction sites NdeI and XhoI for the 5' and 3' end, respectively (Qing et al., 2004). Additional modifications made to the construct include a 6x-His tag and a thrombin cleavage site (LVPRGS) preceding the MCU opening reading frame. Protein expression was determined by Western blot analysis of the total bacterial lysate using mouse anti-His primary antibodies (Qiagen) and HRP-conjugated sheep anti-mouse secondary antibodies (GE Healthcare). For structural studies, the open reading frame of NfMCU (NCBI accession number: XP_001266985.1) was truncated further by 75 residues at the N-terminus and 10 residues from the C-terminus and then re-cloned into the pCOLD II vector using the same restriction sites. These truncations include the 65-residue mitochondrial targeting sequence at the N-terminus of NfMCU and 10 residues each from predicted disordered regions at the N- and C-termini of the channel. These deletions improved the monodispersity of the protein in solution, as judged by size exclusion chromatography (Fig. 4A), and did not significantly affect channel activity (Fig. 4B). All single-site mutants were generated using the Quikchange Site-Directed Mutagenesis Kit (Agilent) and confirmed by DNA sequencing.

E. coli (BL21 DE3) were freshly transformed, plated onto LB/ampicillin (LB/Amp) agar, and grown overnight. Colonies were harvested directly from LB/Amp plates to seed

LB media (supplemented with ampicillin to a final concentration of 100μg/mL) and grown in shaker flasks at 37°C in an orbital shaker until the cells reached an OD_{600} = 0.35-0.4, at which point they were transferred to another orbital shaker pre-chilled to 15°C and allowed to grow for another hour before protein expression was induced by addition of IPTG to a final concentration of 0.4mM. Typically, the cells reached an OD_{600} = 0.65-0.8 when they are induced with IPTG. The bacteria were then grown at 15°C for 16-18 hours before being harvested. The cell pellets were either used immediately for protein purification or flash frozen in liquid nitrogen and stored at -80°C.

To purify NfMCU, the cell pellets were resuspended in lysis buffer (50mM Tris pH 8, 300mM NaCl, 1mM $CaCl_2$), supplemented with protease inhibitors (1 μg/mL each of DNase I, pepstatin, leupeptin and aprotinin) and 1 mM PMSF, and then lysed on ice using an Emulsiflex-C5 cell homogenizer (Avestin). To remove inclusion bodies and aggregated protein, the total cell homogenate was centrifuged at 10,000 x g for 20 minutes at 4°C. The supernatant was harvested and NfMCU was extracted with 1% (w:v) n-dodecyl-β-D-maltopyranoside (DDM, Anatrace) by gentle agitation for 1 hour on ice. After extraction, the supernatant was collected following a 30-minute centrifugation at 21,000 x g at 4°C and then incubated with Ni-NTA resin (Qiagen) with gentle agitation on ice for 1 hour. The resin was collected on a disposable gravity column (Bio-Rad), washed with wash buffer A (lysis buffer + 1mM DDM) for 3 column volumes and then with wash buffer B (lysis buffer + 1mM DDM + 30mM imidazole) for 10 column volumes. NfMCU was eluted with wash buffer C (lysis buffer + 1mM DDM + 300 mM imidazole). Thrombin was added at a ratio of 1 unit of thrombin per 1L culture of bacterial cell pellet; the sample was allowed to incubate at 20°C, overnight, to remove the His-tag. NfMCU is then concentrated and

further purified by size exclusion chromatography on a Superdex 200 10/300 GL column (GE Healthcare) pre-equilibrated with buffer D (20mM HEPES pH 7.5, 300mM NaCl, 1mM $CaCl_2$, 1mM DDM). The main peak, which typically eluted around 11mL, was then collected for further biochemical and structural analysis.

For detergent exchange of NfMCU into amphipol (A8-35 or PMAL-C8), the purified protein was mixed with amphipol at a ratio of 1:3 (w/w, MCU : amphipol) and allowed to mix by rotation at 4^{o}C for 1 hour. Detergent was removed by addition of 100mg of BioBeads (BioRad) to the reaction and allowed to rotate at 4^{o}C for 4 hours. The reaction was exchanged into fresh BioBeads every ~4 hours for a total of 3 times. MCU in amphipol was further purified by size exclusion chromatography on a Superdex 200 10/300 GL column (GE Healthcare) pre-equilibrated with buffer D (20mM Tris pH 8.0, 300mM NaCl, 1mM $CaCl_2$). The main peak, which typically eluted around 11mL, was collected for further biochemical and structural analysis.

Thermal stability assay

To determine the thermal stability of MCU, 50µL aliquots of purified protein was heated to various temperatures in a thermal cycler for 10 minutes and then ramped to 4^{o}C. The sample was then centrifuged at ~20,000 x g for 10 minutes at 4^{o}C to remove denatured/aggregated protein. The supernatant was then analyzed by size exclusion chromatography, and the peak intensity was plotted as a function of temperature to obtain a melting curve.

Crystallization of CrMCU

The NTD and pore domain of MCU from *Chlamydomonas rheinhardtii* or CrMCU (NCBI ref. seq.: XP_001697182.1) was expressed and purified as previously described with the exception that the NTD of CrMCU was purified in the absence of detergent and, therefore, I also excluded detergent extraction from the purification protocol. The construct used to obtain crystals of CrMCU-NTD contains residues $_{59}$A – S$_{165}$, which extends approximately 20 residues into the predicted coiled-coil 1 of CrMCU. The protein was crystallized by the hanging drop vapor diffusion method at 20^{o}C, mixed at an equal ratio (v/v) of protein (4-6mg/mL) to precipitant (14% PEG 6000, 0.1M Tris pH8, 0.3M $MgCl_2$, 9% hexane-2,5-diol). Crystals typically appeared within 3-5 days and grew to full size within 2 weeks. The crystals were cryo-protected in a solution containing the mother liquor supplemented with 20% ethylene glycol and then flash frozen in liquid nitrogen. For phasing experiments, I produced selenomethionine derivatized protein following standard protocol. The protein was expressed and purified as described for the native protein. Selenomethionine CrMCU crystalized in a solution containing 15% PEG 6000, 0.1M Tris pH 8, 0.3M $MgCl_2$ and were cryo-protected in a solution containing the mother liquor supplemented with 20% ethylene glycol before being flash frozen in liquid nitrogen.

CrMCU pore, which constitutes residues A$_{190}$ – K$_{247}$, was expressed and purified as described for NfMCU with the exception that the protein was digested on resin (at 20^{o}C for 16-18 hours with gentle rotation) by addition of 2 units of thrombin per 0.5mL bed volume of NiNTA resin. The protein was eluted using wash buffer A and then further purified by size exclusion chromatography using a Superdex 200 10/300 GL column (GE Healthcare) pre-equilibrated with buffer D (20mM Tris pH 8.0, 300mM NaCl, 1mM $CaCl_2$,

3mM n-decyl-β-D-maltopyranoside (Anatrace)). The main peak, which typically eluted around 13.7mL, was then collected for further biochemical and structural analysis. The CrMCU pore was crystallized as described for CrMCU-NTD with the exception that I used the sitting drop vapor diffusion method and the protein was concentrated to 8-10 mg/mL. Crystals typically appeared in PEG 400 (35-42%), 0.1M glycine pH 9-10, NaCl (0.1-0.3M), n-nonyl-β-D-glucopyranoside (9-15mM, Anatrace) between 3-6 weeks and grew to full size within 3-4 weeks; the crystals were directly harvested from the well mother liquor and flash frozen in liquid nitrogen.

X-ray data collection

Diffraction data of CrMCU-NTD crystals were collected at the Advanced Photon Source beamlines 23-ID-B/D and at the Advanced Light Source beamlines BL8.2.1 and BL8.2.2. All diffraction data were processed and scaled using HKL2000 (Otwinowski, 1997). The structures were determined using Phenix AutoSol on single-wavelength anomalous diffraction datasets from selenomethionine derivatized CrMCU-NTD crystals. The model was built in Coot (Emsley, 2010) and refined in Phenix (Adams, 2010). Table 1 provides a summary of the data collection and refinement statistics for the crystal structure of CrMCU-NTD.

Table 1. Data collection and refinement statistics for CrMCU-NTD

Statistics	CrMCU-NTD (native)
Data Collection	
Space group	P1 21 1
Cell dimensions a, b, c (Å)	48.92, 76.17, 69.07
α, β, γ (°)	90.0, 109.1, 90.0
Wavelength (Å)	1.000
Resolution (Å)	46.2-2.2 (2.29-2.25)
R_{merge} (%)	0.097
Reflections	22581 (2169)
$I/\sigma(I)$	8.5 (2.0)
Completeness (%)	97.9 (94.2)
Refinement	
R_{work}/R_{free}	19.6/23.7
No. of atoms	
Protein	363
Ion	4
Water	270
R.M.S.D.	
Bond angles (°)	0.493
Bond lengths (Å)	0.002
Ramachandran plot	
Favored (%)	98.59
Allowed (%)	1.13
Outliers (%)	0.28
Values in parentheses are for the highest resolution shell. 8.89% of the data were used for R_{free} calculations.	

Reconstitution of NfMCU into nanodisc and saposin

I reconstituted NfMCU into nanodisc following the published protocol but with slight modifications (Denisov, 2004). Our reaction consists of the following components mixed

at a molar ratio of 1:2:10 (NfMCU : MSP1 : *E. coli* total lipid) and then allowed to proceed with gentle rotation at 4^{o}C for 1 hour before addition of BioBeads to remove detergents. The reaction was incubated with BioBeads for 3-4 hours at 4^{o}C, and BioBeads exchange was performed a total of 3 times with each incubation step lasting 3-4 hours at 4^{o}C. The reconstituted NfMCU nanodisc complex was separated from empty nanodiscs and aggregates by gel filtration chromatography on a Superdex 200 10/300 GL column (GE Healthcare) pre-equilibrated with buffer E (20mM HEPES pH 7.5, 300mM NaCl, 1mM $CaCl_2$, 2% glycerol). The main peak (eluting around 11mL) was then collected for structural analysis.

I was unsuccessful in reconstituting NfMCU with saposin following the original protocol (Frauenfeld, 2016), likely due to the recommended step of heat shocking the sample during reconstitution. I thus made some modifications to the protocol, which I believe is better suited for more sensitive or less stable membrane proteins. Our reaction consists of the following components mixed at a molar ratio of 1:3:10 (NfMCU : saposin : E. coli total lipid) and then allowed to proceed with gentle rotation at 4^{o}C for 1 hour before addition of BioBeads to remove detergents. In place of the heat denaturation step to destabilize the saposin molecules, I pre-incubated saposin with *E. coli* total lipid and sodium cholate (15mM final concentration) and allowed the reaction to proceed with gentle rotation at 4^{o}C for ~1 hour. We followed the same protocol for removing detergent as was described previously for the reconstitution of NfMCU into nanodisc.

EM data acquisition

Prior to freezing grids, the NfMCU saposin complex (concentrated to 0.6mg/mL) was incubated with 50μM Ru360 on ice for 30 minutes. The cryo-EM grids were prepared by applying 3 μL of the NfMCU-saposin-Ru360 complex to a glow-discharged Quantifoil R1.2/1.3 300-mesh gold holey carbon grid (Quantifoil, Micro Tools GmbH, Germany) and blotted for 4.0 seconds under 100% humidity at 4 °C before being plunged into liquid ethane using a Mark IV Vitrobot (FEI). Micrographs were acquired on a Titan Krios microscope (FEI) operated at 300 kV with a K2 Summit direct electron detector (Gatan), using a slit width of 20 eV on a GIF-Quantum energy filter as well as a Volta phase plate following the same approach for phase plate data collection as previously described (Danev, 2017). EPU software (FEI) was used for automated data collection following standard FEI procedure. A calibrated magnification of 59,523X was used for imaging, yielding a pixel size of 0.84 Å on images. The defocus was set at -0.5 μm. Each micrograph was dose-fractionated to 30 frames under a dose rate of 4 e^-/pixel/s, with a total exposure time of 12 s, resulting in a total dose of about 60 $e^-/Å^2$.

Image processing

For the NfMCU phase plate dataset, motion correction was performed using the MotionCorr2 program (Zheng, 2017), and the CTF parameters of the micrographs were estimated using the GCTF program (Zhang, 2016). All other steps of image processing were performed using RELION (Scheres, 2012). Initially, about 1,000 particles were manually picked from a few micrographs. Class averages representing projections of

NfMCU in different orientations were selected from the 2D classification of the manually picked particles, and used as templates for automated particle picking from the full data set of 2,470 micrographs. The 526,554 extracted particles were binned 3 times and subjected to two rounds of 2D classification, and a total of 355,929 particles were finally selected for 3D classification using the initial model generated by RELION as the reference. Two of the 3D classes showed good secondary structural features and their particles were selected, combined and re-extracted into the original pixel size of 0.84 Å. After 3D refinement with C2 symmetry imposed and particle polishing, the resulting 3D reconstructions from 128,231 particles yielded an EM-map with a resolution of 3.8 Å. The transmembrane domain showed poor density, indicating local structural heterogeneity. Therefore, focused 3D classification with density subtraction was performed in order to improve the density of the transmembrane domain (Bai et al., 2015). In this approach, the density corresponding to the soluble domains of the channel as well as the belt-like density from saposin was subtracted from the original particles. The subsequent 3D classification on the modified particles was carried out by applying a mask around the transmembrane domain and having all the orientations fixed at the value determined in the initial 3D refinement. After this round of classification, one class (83,343 particles) with better density in the transmembrane domain was selected for 3D refinement, yielding an EM map of 3.8 Å in which the entire transmembrane domain can be modeled. All resolutions were estimated by applying a soft mask around the protein density and the gold-standard Fourier shell correlation (FSC) = 0.143 criterion. ResMap (Kucukelbir, 2014) was used to calculate the local resolution map.

Model building, refinement, and validation

De novo atomic model building was conducted in Coot (Emsley, 2010). Since the crystal structure of the N-terminal domain (NTD) of human MCU (PDB: 4XTB) fits nicely as a rigid body into the NTD of NfMCU, I used the crystal structure as a guide to build the NTD of NfMCU. Amino acid assignment was achieved based on the clearly defined density for bulky residues (Phe, Trp, Tyr, and Arg). Models were refined against summed maps using phenix.real_space_refine (Adams, 2010), with secondary structure restraints applied. The model was validated using previously described methods to avoid overfitting (Amunts, 2014, DiMaio, 2013). The 3.8 Å EM density map of NfMCU allowed me to construct a model containing the following residues: chain A, B: 124-201, 258-399, and 406-461; chain C, D: 124-201, 258-397, and 404-461. The statistics for the model's geometries were generated using MolProbity (Chen, 2010). Pore radii were calculated using the HOLE program (Smart, 1996). All the figures were prepared in PyMol (Schrödinger, 2015) or Chimera (Pettersen, 2005). Table 2 provides a summary of the data collection and refinement statistics for the cryo-EM structure of NfMCU.

Table 2. Cryo-EM data collection, refinement and validation statistics

	NfMCU
Data collection and processing	
Magnification	59,523
Voltage (kV)	300
Electron exposure (e–/Å^2)	60
Defocus range (μm)	-0.5
Pixel size (Å)	0.84
Symmetry imposed	C2
Initial particles (no.)	526,554
Final particles (no.)	128,231
Map resolution (Å)	3.8
FSC threshold	0.143
Map resolution range (Å)	211-3.8
Refinement	
Model resolution (Å)	3.8
FSC threshold	0.143
Model resolution range (Å)	211-3.8
Map sharpening *B* factor (Å^2)	-120
Model composition	
Non-hydrogen atoms	8949
Protein residues	1088
Ligands	1
B factors (Å^2)	116.42
Protein	116.41
Ligand	151.7
R.m.s. deviations	
Bond lengths (Å)	0.01
Bond angles (°)	1.10
Validation	
MolProbity score	2.02
Clashscore	6.76
Poor rotamers (%)	1.68
Ramachandran plot	
Favored (%)	92.29
Allowed (%)	7.71
Disallowed (%)	0

Bacterial calcium uptake assay

E. coli expressing NfMCU were grown as described above with the exception that protein induction was allowed to proceed for 16 hours, at which time the cells were

harvested, centrifuged at 4000 x g for 10 minutes at 4°C, and the media was discarded. To remove residual media, the cell pellet was resuspended in ice-cold buffer (50mM HEPES pH 7.4, 150mM KCl) and then centrifuged again (4000 x g for 10 minutes at 4°C) and the supernatant was discarded. To prepare the bacteria for calcium uptake measurements, the bacteria were treated as though they were mitochondria and prepared as previously described for the purification of mitochondria from yeast (Yaffe, 1991) but with slight modifications. To remove residual Ca^{2+}, the cells were resuspended to a final concentration of 10mg/mL in ice-cold bacteria prep buffer (0.6M D-mannitol, 10mM KH_2PO_4, 20mM HEPES pH 7.4, 5mg/mL bovine serum albumin) plus 1mM EDTA and allowed to shake gently on ice for 30 minutes. To replenish any Mg^{2+} that was chelated by EDTA treatment, 2mM $MgCl_2$ was then added into the cell resuspension followed by gentle shaking on ice for another 30 minutes. The cells were then centrifuged (4000 x g for 10 minutes at 4°C) and the supernatant was discarded. The cells were centrifuged again (4000 x g for 3 minutes at 4°C) and residual buffer was removed with a pipette. The wet weight of the bacteria was measured with a digital balance (typical yield is ~80mg of bacteria per 30mL culture of bacteria). The cells were then resuspended in ice-cold reaction buffer (0.6M D-mannitol, 20mM HEPES pH 6.8, 10μM EGTA, 0.5mg/mL bovine serum albumin) to a final concentration of 10mg/mL and were used immediately for calcium uptake measurement.

To measure calcium uptake, I used the fluorescent calcium indicator Oregon Green BAPTA-6F (Life Technologies), which was added to a final concentration of 1μM (from aliquots of a 500μM stock kept at -20°C) to cells resuspended in reaction buffer, to monitor the Ca^{2+} concentration changes over time using fluorescence signal – a

conventional approach for monitoring mitochondrial calcium uptake in the field (Baughman, 2011, De Stefani, 2011). For calcium uptake measurements, 100μL of cell suspension was added to a 96-well plate (Corning) and fluorescence was monitored in a Molecular Devices SpectraMax M3 plate reader (excitation/emission: 485nm/535nm). Baseline fluorescence was measured for all samples at the start of each reaction for 60 seconds followed by addition of 5μL $CaCl_2$ stock to the 100μL reaction in any experiment to reach the desired concentration. Unless otherwise indicated, the bacteria were pulsed with 50μM $CaCl_2$ (by addition of 5μL of a 1mM $CaCl_2$ stock). Fluorescence was monitored for 4 minutes to assess calcium uptake.

For the inhibition experiments (either with $GdCl_3$ or Ru360), the inhibitor was added to 1000μL of cell suspension to the highest desired concentration of inhibitor for the experiment and this cell suspension was then used as a stock to dilute into a cell suspension without any inhibitor added (to a final volume of 100μL) to obtain a series of cells in the desired inhibitor concentration. The samples were then pulsed with 50μM $CaCl_2$ and fluorescence was monitored for 4 minutes.

To ensure protein expression was comparable among the NfMCU mutants tested in our uptake assay, Western blot analysis was performed on each sample used for each experiment. Figure 17E and 19E show representative Western blots of an experimental trial using the NfMCU mutants referred to in this study. Mouse anti-His antibodies (Qiagen) was used to detect NfMCU expression and mouse anti-E. coli RNA polymerase alpha or anti-RpoA (Santa Cruz Biotechnology) was used as a loading control. HRP-conjugated sheep anti-mouse antibodies were used as the secondary antibodies (GE Healthcare).

All data were analyzed in GraphPad Prism 7 (GraphPad Software, Inc.). To obtain the rate of calcium uptake, the linear phase of the uptake measurement – the first 45-60 seconds of the reaction following $CaCl_2$ administration – was determined by fitting the data to a linear regression equation in GraphPad Prism; the slope of the fit is taken as the rate of calcium uptake. Further analysis such as normalization are indicated in the figure legend. To obtain the IC_{50} for Ru360, the relative calcium uptake rates were fitted to a dose-response curve in GraphPad Prism.

Radioactive $^{45}Ca^{2+}$ flux assay

NfMCU was reconstituted into lipid vesicles using a similar protocol as described (Heginbotham, 1998). *E. coli* total lipid (Avanti) was prepared following standard protocol and then solubilized in dialysis buffer (50mM HEPES pH 7.4, 150mM KCl) supplemented with 40mM n-decyl-β-D-maltopyranoside (DM, Anatrace). Purified NfMCU in DDM (at ~1mg/mL) was mixed with the DM-solubilized *E. coli* total lipid (10mg/mL) at a ratio of 1:100 (w:w, protein : lipids). NfMCU and lipid mixture were incubated with gentle rotation at 4^{o}C for 1 hour and then dialyzed (using dialysis tubing with a molecular weight cutoff of 12,000-14,000 Da, Spectra/Por) against 1L of dialysis buffer at 4^{o}C to remove detergent. Fresh dialysis buffer (1L each time) was exchanged every 18-20 hours for a total of 3 exchanges. Following dialysis, NfMCU proteoliposomes were divided into 100µL aliquots, flash frozen in liquid nitrogen, and stored at -80^{o}C. For all flux assays, three separate batches of bacteria were grown to express NfMCU. The protein was then purified individually and used immediately for reconstitution into liposomes.

The $^{45}Ca^{2+}$ flux assay was performed following the same procedures as previously described but with slight modifications (Heginbotham, 1998). NfMCU proteoliposomes were thawed and sonicated in a bath sonicator for 60 seconds at 15 second intervals before the assay. 100 µL samples were passed through a pre-spun Sephadex G-50 fine gel filtration column (1.5 mL bed volume in a 5 mL disposable spin column) swollen in flux buffer (50 mM HEPES pH 7.4, 150mM KCl or NMDG). The resulting 160 µL of proteoliposome eluent was collected and added to 300 µL of reaction buffer (flux buffer + 0.2µM valinomycin + 83µM $^{45}CaCl_2$) to initiate the reaction. At various time points, 75 µL of this reaction mixture was passed through a pre-spun Sephadex G-50 fine gel filtration column as previously described to remove extra-liposomal ^{45}Ca and stop the flux. The eluent was mixed with 10 mL scintillation cocktail and its radioactivity was measured in a scintillation counter.

For the Ru360 inhibition experiments, NfMCU proteoliposomes in flux buffer (50 mM HEPES pH 7.4, 150mM NMDG) were mixed with reaction buffer containing varying concentrations of Ru360 (dissolved in NMDG flux buffer + 0.2µM valinomycin + 83µM $^{45}CaCl_2$). The reaction was allowed to proceed for 30 minutes, after which the reaction was stopped by passing 75µL of the reaction through a pre-spun Sephadex G-50 fine gel filtration column as previously described. To determine the relative calcium uptake by NfMCU proteoliposomes, the scintillation count for each sample was normalized to the sample without any Ru360 in the reaction.

Antibodies production

Purified NfMCU were reconstituted into liposomes as previously described and the NfMCU proteoliposomes were administered to mice at the Oregon Health and Science University Monoclonal Antibody Core Facility (OHSU) following standard protocols. Conformational specific antibodies were screened using the enzyme-linked immunosorbent assay (ELISA) with purified NfMCU in detergent as the bait and denatured NfMCU as the negative control. In total, seven monoclonal antibodies were produced.

To generate Fab, purified IgG (obtained from OHSU) were diluted to 1mg/mL in phosphate buffered saline, pH 7.0, containing 20mM EDTA, 20mM L-Cystein HCl, 20mM β-mercaptoethanol; papain was added at a ratio of 1:100 (w:w, papain : IgG; reagents from Sigma Aldrich). Digestion was allowed to proceed at room temperature for 4 hours and then stopped by addition of iodoacetamide to 17.5mM (Sigma Aldrich). Fab and Fc fragments were separated by ion exchange chromatography. Papain digested IgG were dialyzed against 1L of ion exchange buffer (20mM Tris, pH 8, 50mM NaCl) at 4^{o}C, overnight and then injected onto a 5mL HiTrap Q Sepharose Fast Flow ion exchange column (GE Healthcare) that was pre-equilibrated with the ion exchange buffer. Fab and Fc were eluted using a linear NaCl gradient from 50mM to 500mM. Eluted fractions were analyzed by Coomassie stained SDS-PAGE and then pooled, aliquoted, flashed frozen in liquid nitrogen, and stored at -80^{o}C for further analysis.

Chapter 3. Structure Determination of MCU

Introduction

Since the molecular identification of MCU, the field has moved at an incredible pace in addressing basic questions pertaining to the function of MCU and its physiological relevance (Kamer, 2015). Sequence analysis shows that MCU is found in all major eukaryotic taxa but absent among many protozoa and fungi (Bick, 2012). Structurally, MCU adopts a unique fold that is characterized by a highly conserved selectivity filter called the DIME motif flanked by transmembrane (TM) and coiled-coil domains. A large amino-terminal domain (NTD) precedes the first coiled-coil but shows low sequence conservation among MCU orthologs (Fig. 2B). Because MCU exhibits no discernible sequence similarity to other ion channels, it poses a major challenge to the use of computational tools to predict structure and function (Bick, 2012).

Nonetheless, structural domains of MCU and its auxiliary subunit have been reported in recent years: the N-terminal domain of human MCU (Lee, 2015), the pore domain of *C. elegans* MCU (Oxenoid, 2016), and human MICU1 (Wang, 2014). While these structures offered the field a glimpse of various isolated domains of the uniplex, they fall short of answering mechanistic questions about the channel's function. For instance, while the crystal structure of the NTD of human MCU showed us the fold of this domain, it does not reveal any information about the possible oligomeric state of the channel. Moreover, it is known that the NTD is poorly conserved among MCU orthologs and secondary structure predictions do not converge on a single fold. Thus, it is possible that the structure of the NTD may indeed vary among MCU homologs.

The recent NMR structure of the pore domain of *C. elegans* MCU or cMCU-ΔNTD, which adopts a pentameric oligomeric state and an occluded ion conduction pathway (Fig. 3A, B), has also generated controversy in the field. First, the oligomeric state of the channel came as a surprise given that there has been no precedent for such an oligomeric state among known calcium selective channels. Voltage-gated calcium channels (Wu, 2015, Wu, 2016), the calcium conducting but non-selective inositol-1,4,5-triphosphate receptor (Fan, 2015) and ryanodine receptor (Yan, 2015), and the calcium selective TRPV6 channel (Saotome, 2016) are tetrameric; the store-operated calcium entry Orai channel is hexameric (Hou, 2012). While it is possible that MCU's oligomeric state is distinct from known calcium selective channels, the structure of cMCU-ΔNTD is also suspicious in that it adopts an occluded pore architecture where five highly electronegative glutamate residues, with their carboxyl sidechains oriented toward the central axis, form the narrowest point along the ion conduction pathway (Fig. 3). First, it is unclear how the channel could possibly adopt such a structure given the energetic unfavorability of having so many negatively charged sidechains clustered at a single locus (Fig. 3A). Second, the protein used in the NMR studies lacked its NTD, which accounts for nearly 50% of the protein sequence; the functional relevance of the NTD, however, is under debate (Lee, 2015, Oxenoid, 2016). Third, the structure of cMCU-ΔNTD was determined in the absence of its auxiliary protein EMRE, which among metazoan MCU is required for function. Although the authors suggest that EMRE may induce a conformational change in the pore to produce a functional channel (Oxenoid, 2016), it is unclear how this would happen. An alternative possibility is that the NMR structure represents a structural artifact of an improperly folded protein given the unusual set of

conditions used by the authors for biochemical and structural studies: cMCU-ΔNTD was overexpressed in *E. coli* and then extracted from inclusion bodies and purified using the denaturing detergent fos-choline 12. Given the absence of any *in vitro* functional data to validate the integrity of the purified protein, it is unclear whether the cMCU-ΔNTD truly represents the native pore architecture of metazoan MCU.

Despite the advances made by the field in recent years, many fundamental questions still remain to be addressed. What does the full-length channel look like? How does it achieve high calcium selectivity while mediating rapid calcium uptake? In this chapter, I describe our efforts to determine the structure of an MCU ortholog from the fungus *Neosartorya fischerii*. The structure reveals the architecture of the ion conducting subunit of the uniplex, its oligomerization, and the structural basis of calcium binding.

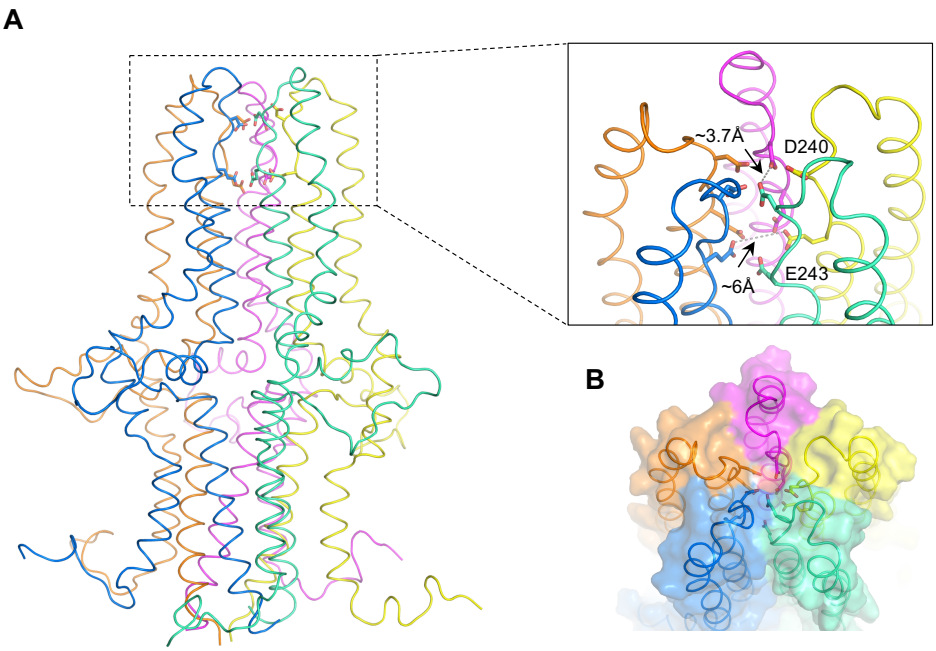

Figure 3. Structure of cMCU-ΔNTD. A, Overall view of cMCU-ΔNTD rendered as ribbon. Each subunit is individually colored with the Asp and Glu of the DIME motif shown as sticks. Inset shows detailed view of the pore entrance of cMCU-ΔNTD with D240 and E243 pointing toward the central axis of the ion conduction pore. The cross distances between opposing carboxylate oxygen atoms at D240 and E243 are indicated. **B**, cMCU-ΔNTD, viewed from the top, is surface rendered to show that the pore entrance is occluded.

Results

Biochemistry and functional assay

Among the 25 MCU orthologs that I screened, those from fungi showed the best expression in *E. coli* and were selected for further characterization. Interestingly, the metazoan MCU orthologs in our screen were poorly expressed or targeted to inclusion bodies, which I suspect is due to their architectural and functional complexity. Among the fungal MCU orthologs that I characterized, the 488-residue wildtype MCU from *Neosartorya fischeri*i, which I call NfMCU, showed the best biochemical properties and was further modified for structural studies. Although the full-length protein can be expressed and purified to milligram quantity, the channel is poly-dispersed in solution, aggregating as high order oligomers (Fig. 4A). Secondary structure prediction analysis shows that the amino- (N-) and carboxy-termini (C-) of NfMCU are disordered, which I suspect might contribute to the polydispersity of NfMCU in solution. Truncating 10 residues each from the N- and C-termini of NfMCU improved the mono-dispersity of NfMCU on gel filtration (Fig. 4A). Additionally, the truncation did not significantly affect the function of the channel, as determined by our bacteria calcium uptake assay (Fig. 4B). SDS-PAGE analysis shows that NfMCU can be purified to homogeneity, and crosslinking experiments show that the channel is indeed tetrameric in solution (Fig. 4C).

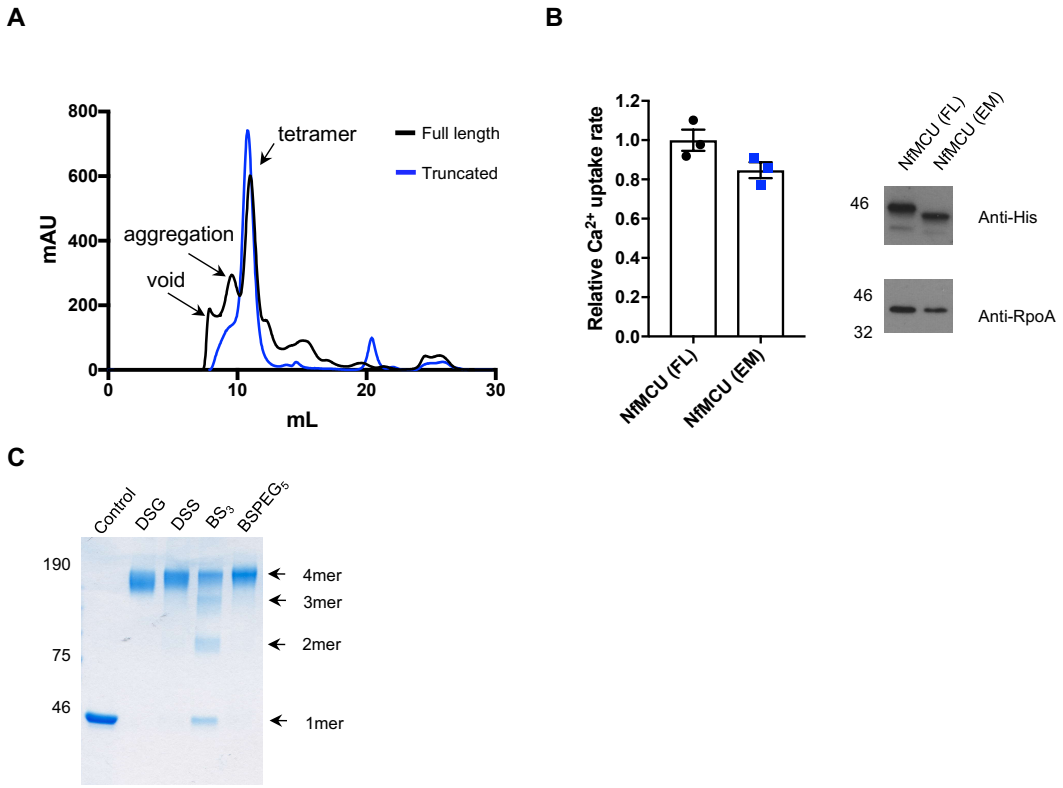

Figure 4. Biochemical analysis of NfMCU. A, Representative gel filtration profile of full-length (black trace) versus truncated NfMCU used for cryo-EM studies (blue trace). **B**, Functional activity of full-length (FL) and truncated NfMCU (EM); data shown represent mean ± SEM, n=3. Cell lysates were analyzed by immunoblotting using anti-His antibody to detect expression of NfMCU; RpoA was used as loading control. **C**, Detergent solubilized NfMCU (control) separates as a single band at ~46kD on Coomassie stained SDS-PAGE and crosslinks as tetramers when treated with chemical crosslinkers of varying spacer arm length. (DSG: disuccinimidyl glutarate, DSS: disuccinimidyl suberate, BS_3: bis(sulfosuccinimidyl) suberate, $BSPEG_5$: PEGylated bis(sulfosuccinimidyl)suberate).

Although mitochondria from the fungus *Neurospora crassa* have been shown to mediate calcium uptake (Carafoli, 1971), direct functional characterization of NfMCU has not been reported. However, a recent report shows that mitochondria from the fungus *Aspergillus fumigatus* can mediate calcium uptake (Song, 2016). Given that *A. fumigatus* contains an MCU ortholog whose sequence shares ~99% identity to that of NfMCU (with 98% sequence coverage), I suspect that mitochondria of *N. fischerii* will likely mediate calcium uptake as well. Nonetheless, I first asked whether heterologously expressed NfMCU can confer uniporter properties to bacteria (see Methodology). As shown in Figure 5A, *E. coli* over-expressing NfMCU cleared repeated pulses of 20μM $CaCl_2$ from the reaction solution while those expressing empty vector exhibited no Ca^{2+} uptake, recapitulating the buffering capacity of purified mitochondria in suspension. The rate of calcium uptake is also concentration dependent, with the rate of calcium uptake plateauing around 80μM $CaCl_2$, which is consistent with the [Ca^{2+}] observed near calcium release sites in cell (Fig. 5B). Additionally, Ca^{2+} uptake can be blocked by sub-micromolar concentrations of the lanthanide Gd^{3+} (Fig. 5C). Finally, the MCU-specific inhibitor Ru360 blocked Ca^{2+} uptake in a dose-dependent manner, with a concentration required to reduce the Ca^{2+} uptake rate by half (or IC_{50}) calculated to be 0.5μM (Fig. 1D). Collectively, these results show that heterologously expressed NfMCU confers uniporter properties to *E. coli* (Gunter, 1990).

In light of the contradiction of the oligomeric state between NfMCU and cMCU-ΔNTD (Fig. 3A and 4C), I next designed an *in vitro* functional assay by reconstituting our purified tetrameric channel into liposomes. Despite numerous attempts, I was unable to measure currents of NfMCU by electrophysiology, which I suspect is due to the channel's

small conductance. Although there has not been any electrophysiology recordings reported for fungal MCU, mammalian MCU currents have been reported, with single channel activity exhibiting multiple subconductance states ranging from 2.5-5pS (Kirichok, 2004). As an alternative approach, I performed a radioactive $^{45}Ca^{2+}$ flux assay on proteoliposomes loaded with 150mM KCl (see Methodology). In a reaction solution containing 150mM NMDG and the K^+-selective ionophore valinomycin (to generate an electrical driving force), NfMCU proteoliposomes exhibited time-dependent $^{45}Ca^{2+}$ uptake while the same proteoliposomes in a reaction solution containing valinomycin and 150mM KCl (to eliminate electrical driving force) accumulated $^{45}Ca^{2+}$ only slightly better than empty liposomes (Fig. 5E), thus recapitulating the voltage-dependent Ca^{2+} uptake property of the MCU. Pharmacologically, Ru360 also blocked NfMCU $^{45}Ca^{2+}$ uptake in a concentration-dependent manner (Fig. 5F) – up to 50%, which is expected if we assume an equal, random distribution of two channel orientations in the liposomes during reconstitution. Therefore, the reconstituted protein forms intact channels that qualitatively recapitulate known properties of MCU and complements results from our bacteria calcium uptake assay.

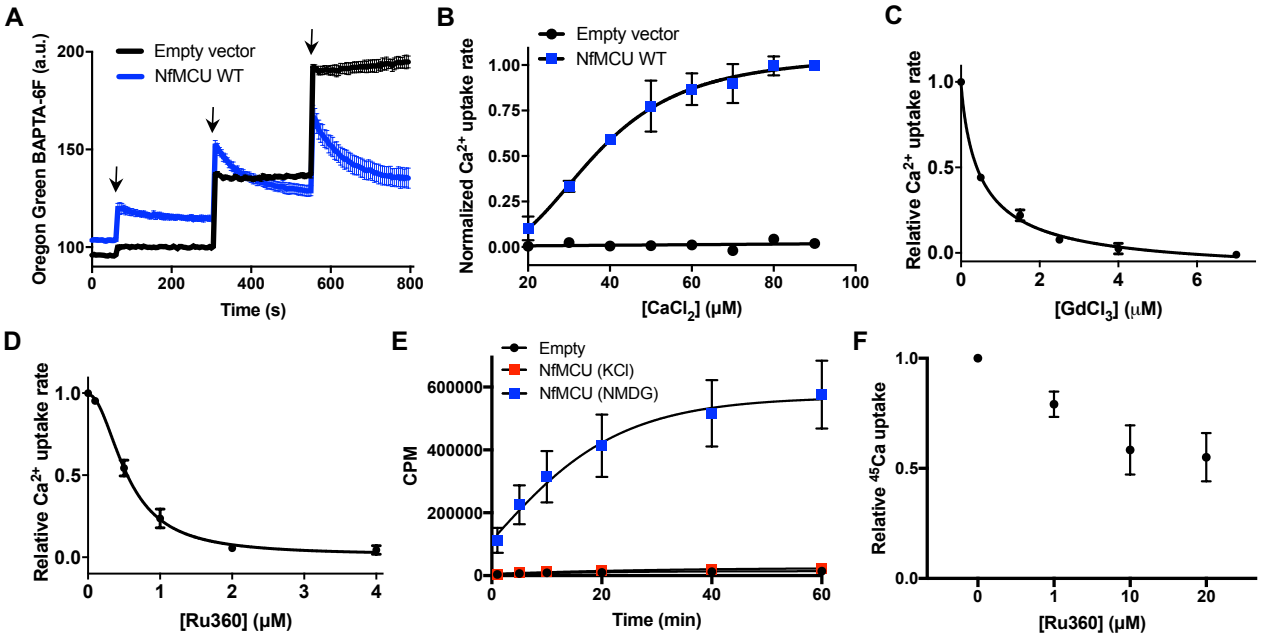
A
Empty vector
NfMCU WT
Oregon Green BAPTA-6F (a.u.)
Time (s)
B
Empty vector
NfMCU WT
Normalized Ca2+ uptake rate
[CaCl2] (μM)
C
Relative Ca2+ uptake rate
[GdCl3] (μM)
D
Relative Ca2+ uptake rate
[Ru360] (μM)
E
Empty
NfMCU (KCl)
NfMCU (NMDG)
CPM
Time (min)
F
Relative 45Ca uptake
[Ru360] (μM)

Figure 5. In vitro reconstitution of NfMCU. A, Calcium uptake in E. coli expressing empty vector (black trace) or NfMCU (blue trace). Arrow indicate addition of 20μM $CaCl_2$ to reaction solution. **B**, Concentration dependent calcium uptake in E. coli expressing empty vector (black trace) or NfMCU (blue trace). Each point represents rate of calcium uptake normalized to the uptake rate at 90μM $CaCl_2$. **C**, Concentration dependent inhibition of NfMCU by $GdCl_3$ in E. coli expressing NfMCU. Each point represents rate of calcium uptake normalized to the uptake rate without $GdCl_3$ in the reaction. **D**, Concentration dependent inhibition of NfMCU by Ru360 in E. coli expressing NfMCU. Each point represents rate of calcium uptake normalized to the uptake rate without Ru360 in the reaction. **E**, Radioactive ^{45}Ca uptake in NfMCU proteoliposomes. Calcium uptake by empty liposomes or NfMCU proteoliposomes incubated with ^{45}Ca in a reaction buffer containing 150mM KCl (red points) or 150mM NMDG (blue points). **F**, Concentration dependent inhibition of NfMCU proteoliposomes by Ru360. Each point represents radioactivity measured following 30 min reaction normalized to sample without Ru360. Note: All data shown represent average ± SEM, n=3.

Structure determination

Crystallization of MCU

I initially attempted to determine the structure of NfMCU using X-ray crystallography. Despite screening extensively for constructs, detergents, and

crystallization conditions, NfMCU failed to produce any crystals. However, I also discovered that NfMCU is a biochemically robust protein. First, NfMCU is stable in a broad range of detergents. In fact, the channel is as stable in the harsher detergent lauryldimethylamine-N-oxide (LDAO) as it is in the mild detergent n-dodecyl-β-D-maltopyranoside (DDM). Second, the channel maintains a stable oligomeric state in DDM for at least 6 months following purification when stored at 4^{o}C. As with previous experiments, I assessed protein stability using size exclusion chromatography or SEC (to assess oligomeric state) and Coomassie stained SDS-PAGE (to assess protein degradation). I also generated monoclonal antibodies against NfMCU to use as molecular chaperones for crystallization. Monoclonal antibodies fragments have been used extensively as a tool for trapping proteins in a specific conformation as well as introduce additional surfaces for crystal contacts to occur, both of which, in theory, should improve the chances of obtaining well-diffracting crystals (Zhou, 2001). Using the purified monoclonal antibodies, I generated Fab following standard protocol (Methodology). The NfMCU-Fab complex showed monodispersity on gel filtration and the peak fraction was collected and screened for crystals. In total, I screened 5 different NfMCU-Fab complexes; however, none of these samples produced any hits in our sparse matrix crystal screens.

I also took a reductionist approach and asked whether I can determine the structure of isolated domains of MCU with the goal of using these structures as templates to rationally design new constructs that are better suited for crystallization. I designed two sets of constructs: one encompassing the amino-terminal domain (NTD) and the other consisting of the pore domain, which constitutes the DIME motif and the transmembrane and coiled-coil domains. Given the low sequence conservation in the NTD among MCU

orthologs, I asked whether this is also reflected in their three-dimensional structures. On the contrary, the pore domain is highly conserved among MCU orthologs and constitute the ion conduction pathway of MCU, which I suspect would provide valuable insights into the mechanism of ion binding and selectivity. I screened all 25 MCU orthologs for protein expression of the NTD and pore domain separately and identified an MCU ortholog from the algae *Chlamydomonas rheinhardtii* or CrMCU, whose NTD and pore domain can be expressed to high levels even though the full-length protein did not express in *E. coli*. The NTD of several fungal MCU orthologs also expressed to high levels but not their pore domain. SEC analysis of these constructs showed that the NTD of fungal MCU orthologs oligomerized in a concentration dependent manner in solution. Varying the salt concentration (0.1 – 0.7M NaCl) or supplementing the buffer with additives (such as reducing reagents and detergents) did not affect the concentration-dependent oligomerization. Nonetheless, I used the purified protein to screen for crystals but were unsuccessful in obtaining any hits, which I suspect is a result of sample heterogeneity in solution.

However, the NTD of CrMCU (or CrMCU-NTD) formed crystals that diffracted X-ray to 2.3 Å resolution (Table 1). I initially attempted to solve the phase problem by molecular replacement using the crystal structure of the NTD of human MCU (PDB: 4XTB) as the search model but could not obtain a solution. Next, I solved the phase problem by single-wavelength anomalous diffraction (SAD) phasing using selenomethionine derivatized crystals (see Methodology). The map was of sufficient quality for me to build an atomic model consisting of residues $_{72}$F – L$_{157}$ (Fig. 6) and refined to an R_{free} = 22.7%. Unlike the crystal structure of the NTD of human MCU (or HsMCU-NTD), which adopts a

barrel fold consisting of seven β-strands and an α-helix with a second α-helix capping the barrel, CrMCU-NTD is a three-helical bundle capped by three anti-parallel β-strands (Fig. 6A). A search of the PDBeFold database (Krissinel, 2004) identified CrMCU-NTD as being structurally related to proteins belonging to the SCOP superfamily of winged-helix DNA-binding domains (Fox, 2014). Furthermore, CrMCU has not been functionally characterized; thus, it is unclear what physiological role it plays *in vivo* or whether CrMCU is functional on its own. Since I was unable to express the full-length CrMCU channel in bacteria, I was unable to probe the functional relevance of the protein further. Interestingly, CrMCU-NTD forms a symmetry related tetrameric ring in the crystal, which offered me a glimpse at the potential oligomerization of MCU at the NTD (Fig. 6B, C).

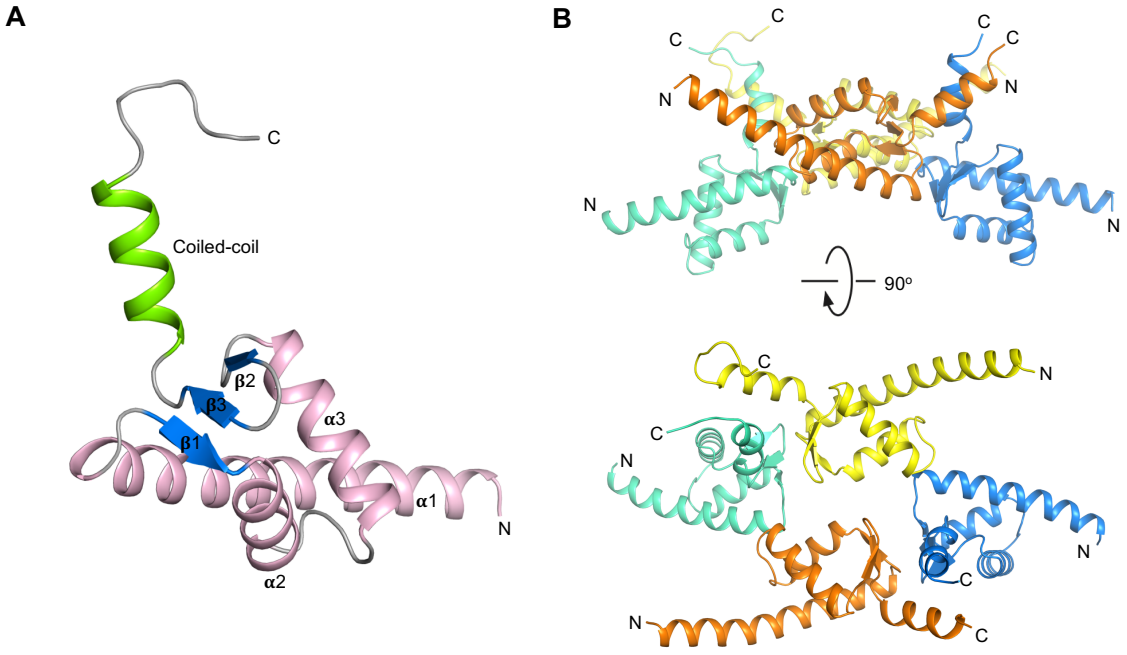

Figure 6. Crystal structure of CrMCU-NTD. A, Overall structure of CrMCU-NTD. Secondary structures are colored following the color scheme used for the NTD of human MCU and NfMCU. **B**, CrMCU-NTD forms a symmetry related tetrameric ring in the crystal lattice. Shown are side view (top panel) and top view (bottom panel) of the ring. Each protomer is individually colored and the N- and C-termini are labeled.

I also succeeded in obtaining crystals of the pore domain of CrMCU (or CrMCU pore). However, the CrMCU pore crystals diffracted X-rays anisotropically, with initial crystals diffracting X-rays to 15-25 Å resolution. I sought to improve the quality of the crystals by the following approach: 1) I modified the construct by lengthening or

shortening the N- and C- termini, which I had hoped would improve protein packing within the crystal lattice. 2) I performed alanine and leucine scans along the transmembrane helices to identify thermal stable mutants. In this approach, small residues (such as glycine, proline, serine, alanine, valine, isoleucine, aspartate, asparagine and threonine) were mutated to leucine while larger residues (such as leucine, arginine, glutamate, glutamine, phenylalanine, tryptophan, and tyrosine) were mutated to alanine. 3) I extensively screened for mixed detergents and additives to improve crystal packing with the rationale that CrMCU pore is mostly buried in detergent micelles and that subtle changes to the detergent micelle can have drastic effects on crystal packing. 4) I tested crystal dehydration, which reduces the solvent content of the crystal and can potentially change protein packing to improve crystal diffraction (Russi, 2011).

Among these attempts, the use of mixed detergent and crystal dehydration most significantly improved the crystal quality. Addition of the short chain detergent n-nonyl-β-D-glucopyranoside (or NG) improved the diffraction to 7-15 Å resolution. Crystal dehydration further improved the severe anisotropic diffraction to 4-8 Å resolution. A complete native dataset for CrMCU pore was processed and scaled to ~7 Å resolution (with the P4 spacegroup assigned). Although we attempted to solve the phase by molecular replacement (Phenix) using various fragments of the NMR structure of cMCU-ΔNTD as the search model, we were ultimately unable to obtain any reliable solution, as determined by the reported Z-score, log-likelihood gain score, and examination of the electron density map. We also attempted to solve the phase by SAD phasing using selenomethionine derivatized protein. Despite several attempts, the protein failed to crystallize. It is worth noting that native crystals of CrMCU pore were extremely difficult to

reproduce; these crystals were typically small (~50 x 50μm), fragile, and took 1-2 months to grow. Although we found a single CrMCU pore mutant (T197L) in our leucine scan that improved the protein's thermal stability from 45^{o}C to 65^{o}C, this mutant also did not crystallize. Additionally, construct modification had little effect on improving crystal quality; only constructs containing 4-5 residues deleted from the N- and C-termini of the original construct ($_{189}$A – K$_{247}$) still crystallized.

Cryo-EM studies on NfMCU

Although I failed to obtain crystals of NfMCU, the protein was biochemically promising and of sufficient size for structure determination by single particle cryo-electron microscopy (cryo-EM). Initial micrographs of NfMCU by negative stain EM showed that the protein is mono-dispersed and randomly oriented on the EM grids. I then proceeded to determine the structure of NfMCU using single particle cryo-EM, which proved to be technically challenging. Accurate particle alignment proved to be major issue because of the small protein size of 180kDa for a channel tetramer, symmetry mismatch between the transmembrane pore and the soluble domains, and an elongated shape with minimal features. Furthermore, NfMCU exhibited non-ideal behaviors for cryo-EM, with detergent solubilized protein aggregating when frozen and those in amphipols exhibiting orientation bias. Given the small protein size of the channel, I sought to improve the signal to noise ratio by collecting data on our NfMCU-Fab complexes, which would increase the molecular weight from ~180kD to ~380kD. Although negative stained micrographs of

NfMCU-Fab showed many side views (Fig. 7A), the frozen samples exhibited severe orientation bias with 2D class averages showing mostly top views (Fig. 7B).

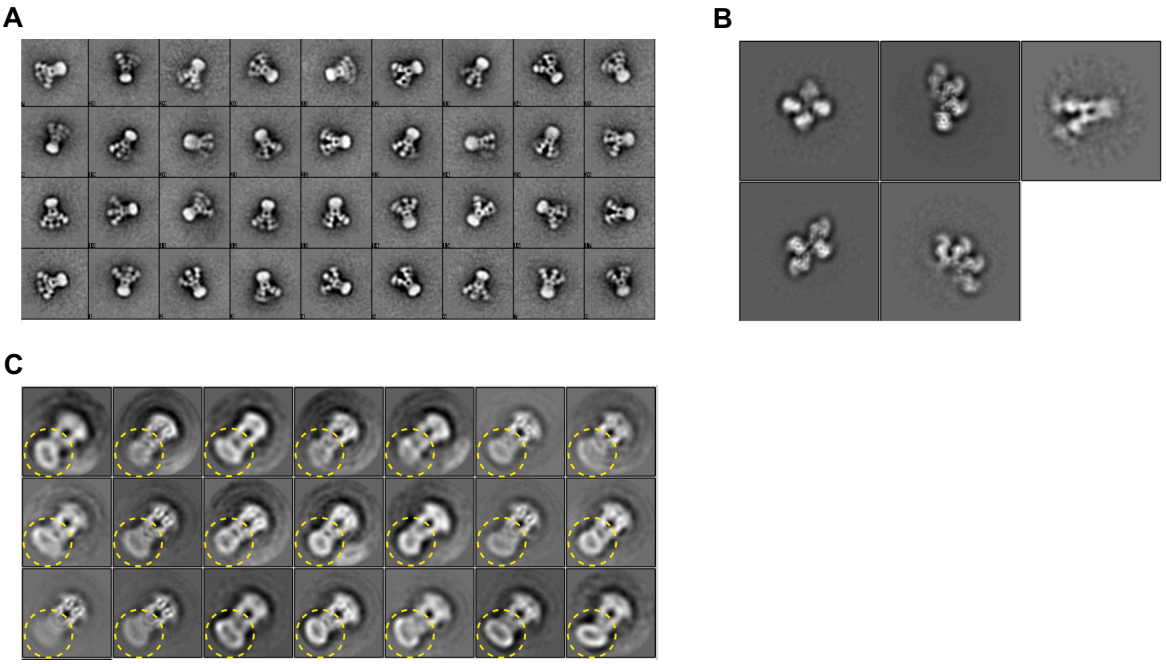

Figure 7. EM analysis of NfMCU in nanodisc. A, 2D class averages of negative stained NfMCU-Fab complex in nanodisc, showing the protein in multiple side views. **B**, 2D class averages of cryo-EM data on NfMCU-Fab complex in nanodisc, which adopts mostly the top view orientation in vitreous ice. **C**, 2D class averages of cryo-EM data on NfMCU in nanodisc. Note the absence of visible secondary structures in the transmembrane domain, highlighted by yellow dashed circles.

Multiple approaches were taken for successful structure determination of NfMCU. I first overcame the stability issue by reconstituting the channel into nanodiscs but, owing to the channel's flexibility in nanodiscs, whose size is much larger than the transmembrane part of the channel, I could only determine the structure to ~15 Å resolution (Fig. 7C). This led me to consider using the newly developed scaffolding protein saposin for reconstitution (see Methodology) (Frauenfeld, 2016), which I rationalized could adapt its oligomerization to maintain NfMCU in an artificial lipid bilayer that is proportional to the channel's smaller transmembrane domain. NfMCU reconstituted in saposin markedly improved the structure to an overall resolution of 4.6 Å (Fig. 8); however, several parts of the channel, particularly the transmembrane domain and the region connecting the coiled-coil to the transmembrane helices, were poorly resolved, likely due to inaccurate particle alignment stemming from the inherently low contrast of small particles (Fig. 8B). Finally, I used a Volta phase plate to image the NfMCU saposin complex, which ultimately allowed me to determine the structure to an overall resolution of 3.8 Å according to the gold-standard Fourier shell correlation 0.143 criterion (Fig. 9). As shown in Figure 9B, the use of the phase plate markedly improved the 2D class averages of NfMCU, which clearly show electron density for the transmembrane domain (TMD) as well as the region connecting the coiled-coil domain (CCD) to the TM helices – features that were not visible in the 4.6 Å cryo-EM structure (Fig. 8). Nonetheless, relative to the rest of the channel, electron density for the TMD was still weak, which suggests conformational heterogeneity in the particles used for 3D reconstruction. Thus, a focused classification on the TMD was performed (see Methodology and Fig. 9C), which removed

44,888 particles that contributed to the heterogeneity of the single particle 3D reconstruction.

Consistent with the biochemical analysis of NfMCU in detergent, the EM map unambiguously shows tetrameric assembly of NfMCU (Fig. 10A). The map was of sufficient quality for me to assign side chains to most of the protein (Fig. 11) although two regions could not be modeled due to disordered electron density: a loop in the NTD ($_{201}$D – E_{257}) and a stretch of 6 amino acids in the juxtamembrane loop (see Methodology). Additionally, the crystal structure of the NTD of human MCU (Lee, 2015) (PDB: 4XTB) fits nicely in the EM map, facilitating the model building of NfMCU-NTD. Parts of the N- and C-termini as well as the long loop in the NTD were disordered and were not modeled in the final structure of NfMCU (Methodology). The EM map also revealed clear electron density for the 81-residue scaffolding protein saposin, which I modeled as poly-alanine (Fig. 12). Six saposin molecules – each forming a C-shaped clamp oriented at a ~45^{o} angle to the central axis – encircle the lipid bilayer to stabilize NfMCU. Thus, for the first time, our structure also reveals how saposin oligomerizes to maintain a membrane protein in a lipid disc.

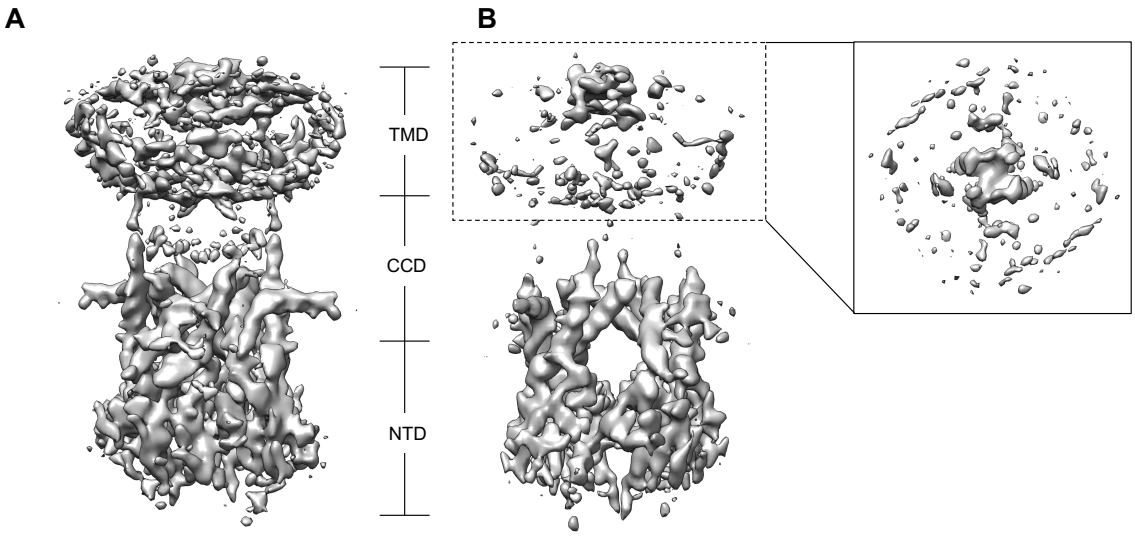

Figure 8. Cryo-EM structure of NfMCU in saposin at 4.6Å resolution. A, Overall structure of NfMCU. The electron density was of sufficient quality to define major domains within the protein: NTD (amino terminal domain), CCD (coiled-coil domain), TMD (transmembrane domain). **B**, Electron density for the TMD and the region proximal to the TMD are poorly resolved. Inset shows a top view of NfMCU's pore domain. Electron density for the transmembrane helices can be observed but their connectivity was ambiguous.

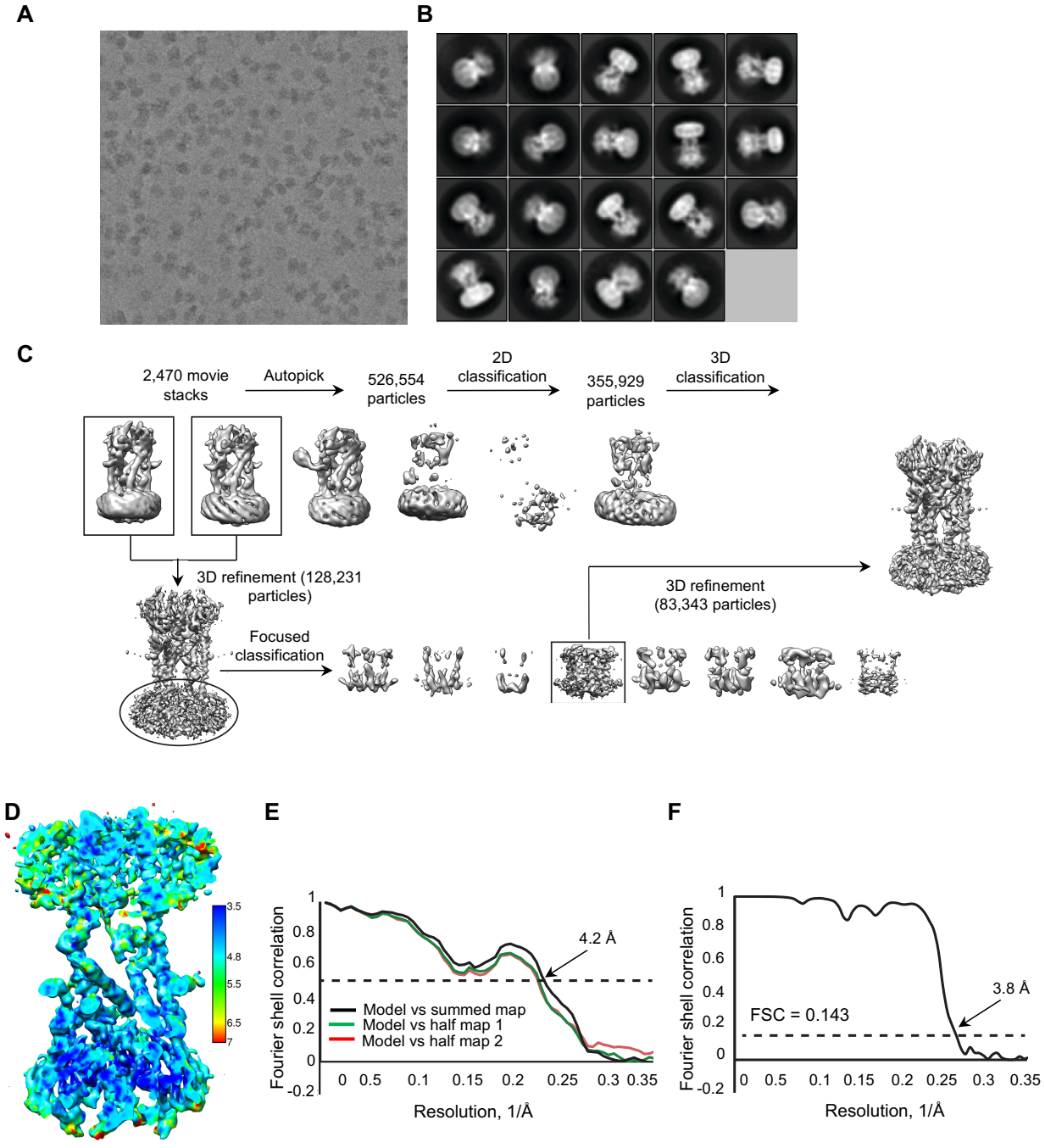
A
B
C
2,470 movie stacks
Autopick
526,554 particles
2D classification
355,929 particles
3D classification
3D refinement (128,231 particles)
Focused classification
3D refinement (83,343 particles)
D
3.5
4.8
5.5
6.5
7
E
Fourier shell correlation
4.2 Å
Model vs summed map
Model vs half map 1
Model vs half map 2
Resolution, 1/Å
F
Fourier shell correlation
FSC = 0.143
3.8 Å
Resolution, 1/Å

Figure 9. Cryo-EM analysis of NfMCU. A, Representative phase-plate electron micrograph of the NfMCU saposin complex. **B**, Representative 2D class averages of the NfMCU saposin complex. **C**, Flowchart of data processing to obtain the 3.8 Å cryo-EM map of the NfMCU saposin complex. Details can be found in the "Image processing" section of the Methods. **D**, Local resolution of NfMCU estimated with RELION2.0. **E**, FSC curves for the refined model versus the summed 3.8 Å map (black curve), the refined model versus half map 1 (red curve), and the refined model versus half map 2 that was not used for refinement (green curve). **F**, The gold-standard Fourier shell correlation curve for the cryo-EM map.

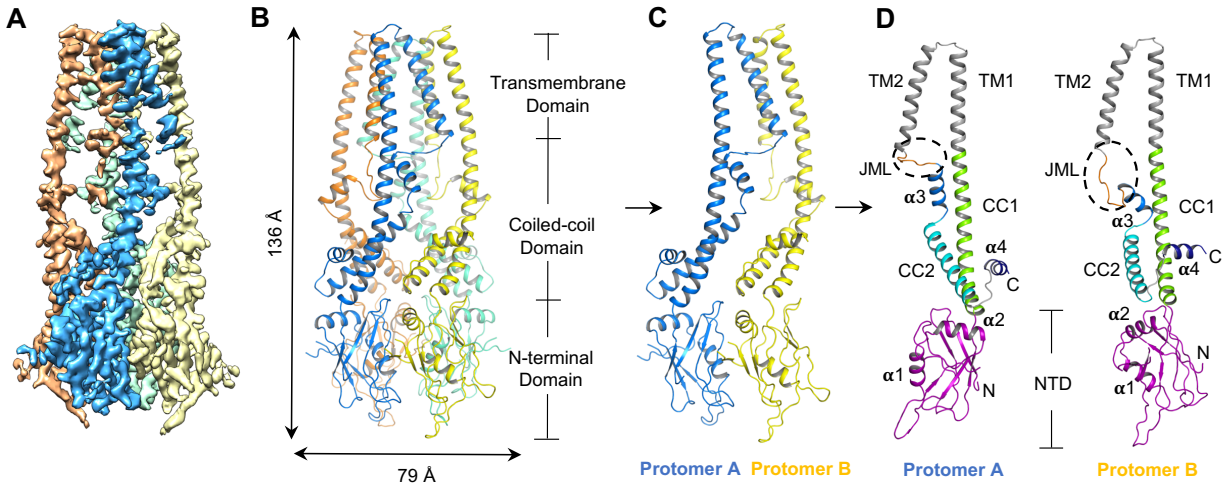

Figure 10. Cryo-EM structure of NfMCU. A, The overall cryo-EM map of NfMCU with density for saposin removed for clarity. **B**, Overall architecture of NfMCU colored by subunit and divided into major structural domains. **C**, Each NfMCU tetramer assembles as a dimer of dimer. Each dimer consists of two protomers with distinct conformation. **D**, Each MCU dimer is divided into individual subunits and are colored and labeled according to their structural features. Dashed circles highlight the distinct conformation of the juxtamembrane loop (JML) in the two protomers.

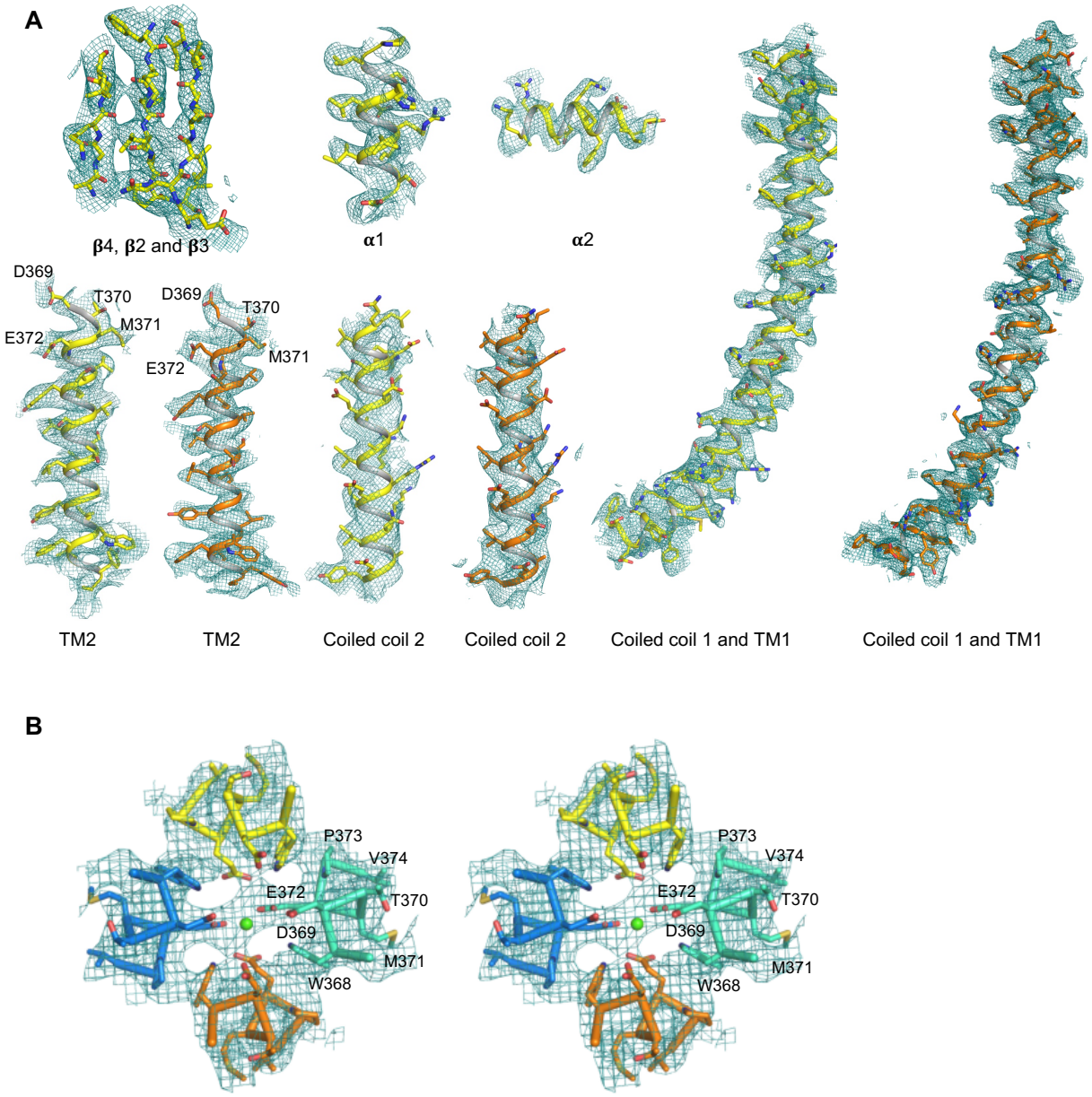

Figure 11. EM map of NfMCU. A, Representative regions of the EM map of NfMCU highlighting key structural features at the NTD (α1, α2, β2-β3), the coiled-coil domain, and transmembrane domain (TM1 and TM2). Protomer 1 and 2 are shown in yellow and orange, respectively. The DIME motif is labeled in TM2. **B**, Stereo view of the EM map carved around TM2s of NfMCU.

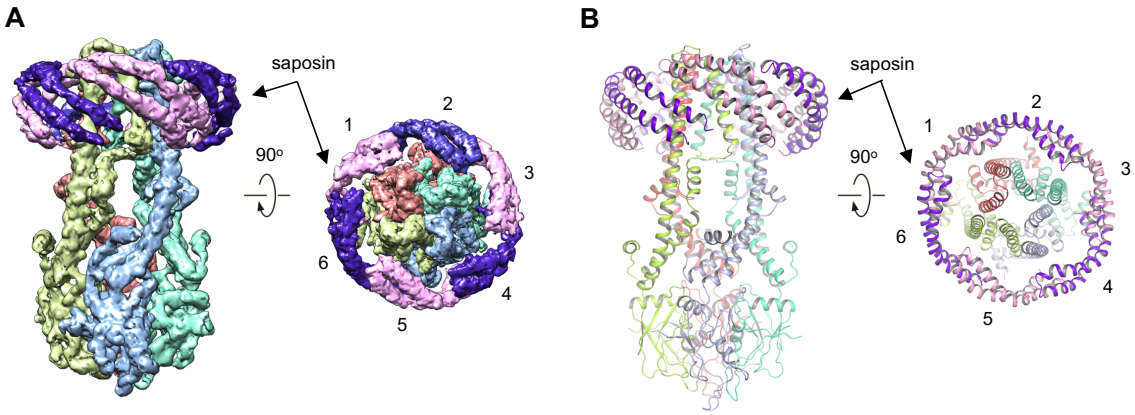

Figure 12. Cryo-EM structure of NfMCU in complex with saposin. A, Cryo-EM map of NfMCU in complex with saposin (shown alternating between purple and pink). Six saposin molecules, each oriented at a 45° angle to the vertical axis, wrap around NfMCU stabilized in lipid. **B**, Ribbon diagram of NfMCU in complex with saposin. Approximately 79-80 residues of the 81-residue saposin molecule was modeled as a poly-alanine chain into the helix-turn-helix EM map density for saposin.

Overall architecture of NfMCU

NfMCU forms an elongated, three-tiered channel tetramer with each tier corresponding to a structural domain, namely the N-terminal domain (NTD), the coiled coil domain (CCD) and the transmembrane domain (TMD) (Fig. 10B). The NTD and TMD define the bottom and top tier, respectively, with the CCD positioned in between. Although NfMCU is a tetrameric channel, it transitions from being four-fold symmetric at the TMD to being two-fold symmetric in the NTD, which forms a dimer of dimer (Fig. 10C, 13A). Unlike the NMR structure of cMCU-ΔNTD, which adopts a constricted architecture, the EM structure of NfMCU is architecturally open, with large fenestrations occupying most

of the space defined by the CCD (Fig. 14A). The middle tier CCD resembles pillars supporting the TMD, with the NTD serving as the foundation. The tight packing among the four NTD subunits, as well as the exceptionally long CC1 helix that extends continuously into TM1 (Fig. 10D), dictates the spacing among the four CCDs, thereby, creating a highly solvent accessible space directly below the ion conduction pathway.

There are several major differences between the EM structure of NfMCU and the NMR structure of cMCU-ΔNTD whose NTD was deleted. In addition to the above mentioned oligomeric state and the overall architecture of the channel (Fig. 14A), the secondary structural elements between the two structures are also quite different. For example, the CC1 and TM1 is a single extended helix in the EM structure but become five short broken helices in the NMR structure (Fig. 14B). These structural differences are unlikely to be caused by the different origins of the two channels, as the CCD, TMD and selectivity filter are highly conserved among MCU orthologs (Bick, 2012) (Fig. 15). I suspect that the missing NTD and the use of a denaturing detergent like fos-choline to extract and purify protein from inclusion bodies in the NMR study contributed to the discrepancy.

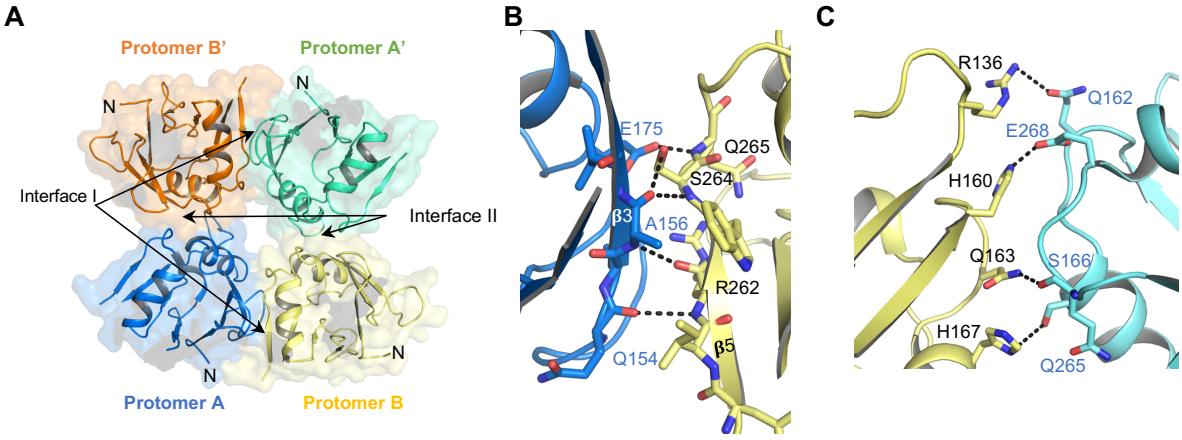

Figure 13. Channel assembly and subunit interfaces at the NTD. A, Top view of surface rendered NfMCU showing intersubunit interactions at the NTD. Each MCU dimer interacts through interface I and tetrameric assembly is mediated by interface II. **B**, Detailed view of atomic interactions at interface 1 in NfMCU consisting of hydrogen bonds mainly between main chain atoms. **C**, Atomic interactions at interface 2 consist of mainly side chain hydrogen bonds.

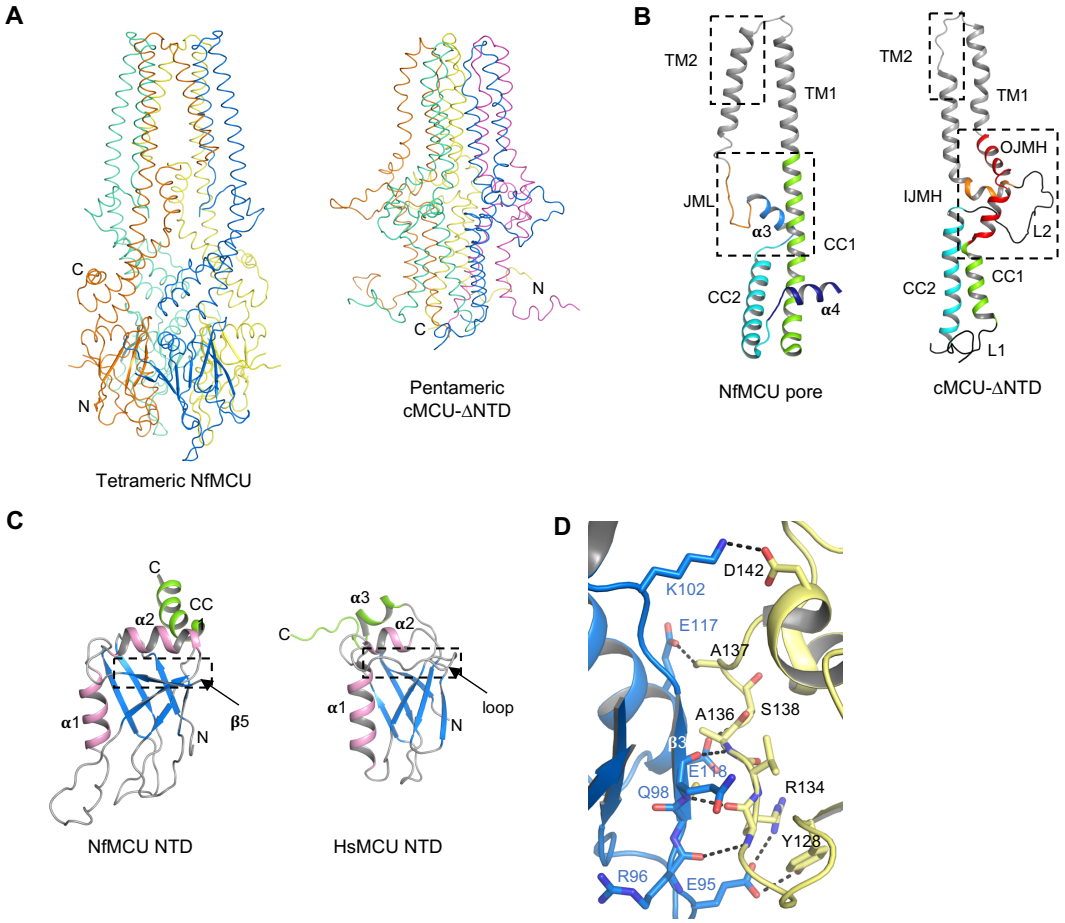

Figure 14. Structure comparison between MCU domains. A, Overall structure comparison between tetrameric NfMCU and pentameric cMCU-ΔNTD (PDB: 5ID3). **B**, Structure comparison between the pore domain of NfMCU and cMCU-ΔNTD. Dashed boxes indicate major differences between the two structures. Structural features in cMCU-ΔNTD are labeled as in the original structure. (IJMH: inner juxtamembrane helix, OJMH: outer juxtamembrane helix, L1: loop 1, L2: loop 2, JML: juxtamembrane loop, CC1: coiled-coil 1, CC2: coiled coil 2). **C**, Structure comparison between the NTD of NfMCU and HsMCU (PDB: 4XTB). Dashed box indicates major difference between the two structures. **D,** Atomic interactions between NTD dimers in the crystal structure of HsMCU NTD at the primary interface identified in the cryo-EM structure of NfMCU.

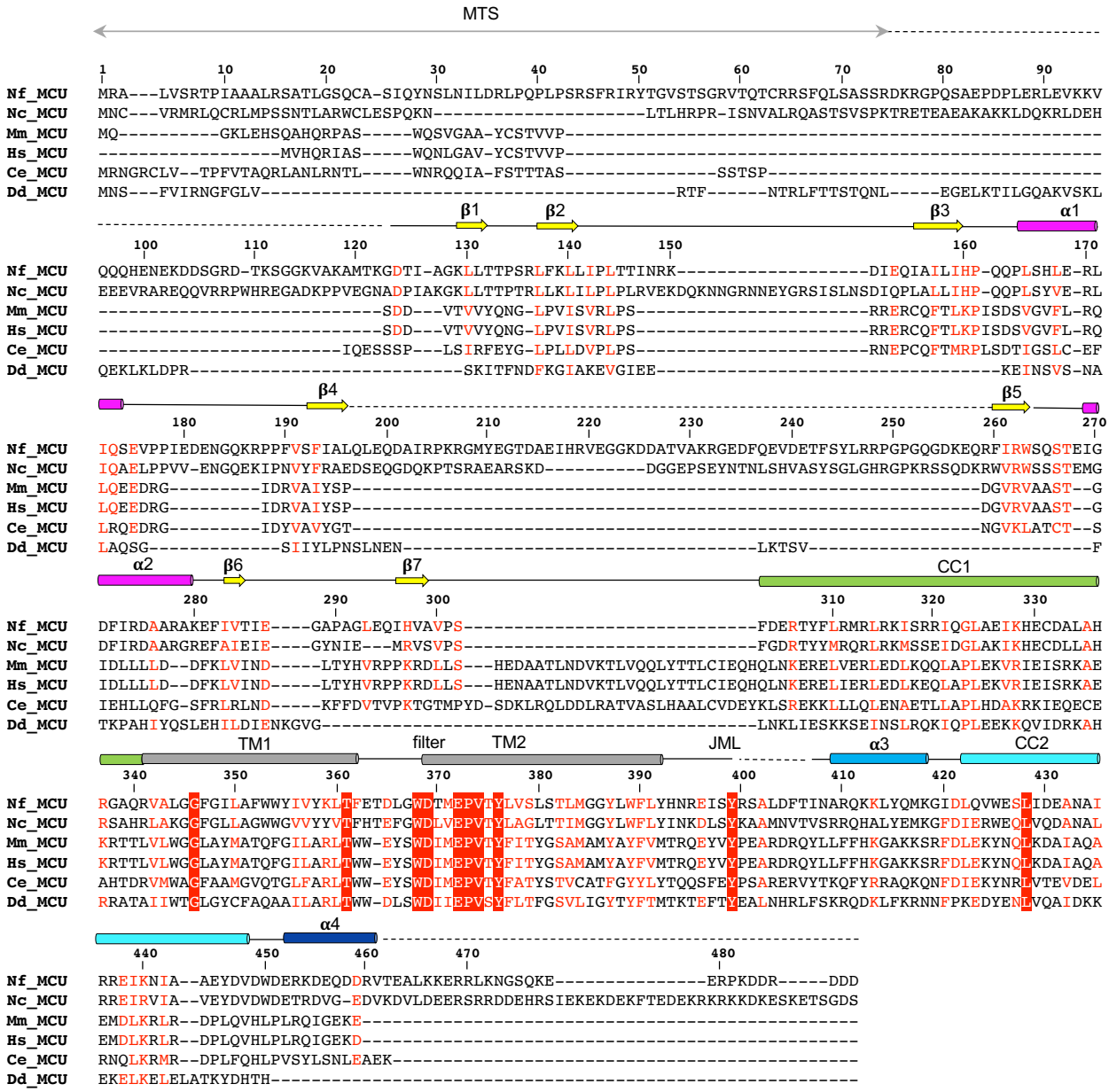
MTS
Nf_MCU
Nc_MCU
Mm_MCU
Hs_MCU
Ce_MCU
Dd_MCU
β1
β2
β3
α1
β4
β5
α2
β6
β7
CC1
TM1
filter
TM2
JML
α3
CC2
α4

Figure 15. Sequence alignment of MCU orthologs. The sequences were aligned using PROMALS3D and numbered according to NfMCU. Secondary structures shown above the sequences are based on the cryo-EM structure of NfMCU. Loops are denoted by solid black lines; disordered regions not observed in the cryo-EM structure of NfMCU are indicated by dashed lines; and the first 75 residues in NfMCU (grey arrow) are predicted to be the mitochondrial targeting sequence (MTS). NCBI accession number for the sequences are: [HsMCU (human MCU): NP_612366.1, MmMCU (mouse MCU): XP_006513531.1, DdMCU (*Dictyostelium discoideum* MCU): XP_637750.1, CeMCU (*C. elegans* MCU): NP_500892.1, NcMCU (*Neurospora crassa* MCU): XP_959658.1, NfMCU (*Neosartorya fischerii* MCU): XP_001266985.1].

Luminal soluble domains

The NTD and CCD constitute the luminal soluble domains of NfMCU. Despite the poor sequence conservation of the NTD among MCU orthologs (Bick, 2012) (Fig. 15), NfMCU-NTD shares a similar structure to that of the NTD from human MCU. Consisting of seven beta stands (β1-7) and two helices (α1 and 2), each NTD forms a barrel enclosed by the 7-stranded β sheet and α1 helix with the α2 helix sitting atop the barrel (Fig. 14C). This is in stark contrast to the previously determined crystal structure of the NTD of CrMCU from algae (Fig. 6A). Four NTDs form a well-packed tetrameric ring in a dimer of dimer configuration with two-fold symmetry (Fig. 13A). Inter-subunit interactions are defined by two types of interfaces. One interface involves primarily hydrogen bonding between main chain atoms on β5 of one subunit and β3 of a neighboring subunit, which I refer to as interface I (Fig. 13B). The other interface is stabilized by hydrogen bonding

between polar side chains (Fig. 13C), which I refer to as interface II. It is worth noting that a similar dimerization at interface I is also observed in the crystal structure of HsMCU-NTD (Fig. 14D), thus highlighting the structural conservation of NfMCU to human MCU. The tetrameric assembly of the NTD implies its crucial role in maintaining the channel's architectural integrity. However, its functional importance is not entirely clear based on functional studies done on human MCU. Structural studies on the NTD of human MCU suggests that the NTD is necessary for efficient mitochondrial calcium uptake (Lee, 2015). On the other hand, it has also been shown that the NTD of human MCU is dispensable – not affecting protein expression or calcium uptake in MCU-knockout HEK cells (Oxenoid, 2016). Thus, the relevance of the NTD of MCU warrants further investigation.

The CCD consists of four helices labeled as CC1, α3, CC2 and α4 (Fig. 10D, 15). The first coiled-coil (CC1) forms an exceptionally long alpha helix that curves with respect to the central axis as it extends from the NTD toward the TMD – transitioning seamlessly into TM1 as it enters the lipid bilayer. A juxtamembrane loop (JML) – approximately 10 residues – and the α3 helix connect the end of the TM2 helix to the second coiled-coil (CC2) in two distinct conformations between two neighboring subunits (Fig. 10D). In one subunit, the loop runs parallel to the membrane and the α3 helix runs almost parallel to CC1, while in the other subunit the loop extends nearly perpendicularly from the membrane and the α3 helix becomes more perpendicular to CC1. The CC2 helix runs nearly parallel to CC1 to form a coiled-coil and the CCD ends with the short α4 helix that runs perpendicularly to the coiled-coil, jutting away from the central axis (Fig. 10D).

Ion-conducting pore

The pore of NfMCU is architecturally unique as compared to classical 2-TM tetrameric cation channels like KcsA (Doyle, 1998), in which the outer TM1 helix wraps around the inner pore forming TM2 helix and generates an inverted teepee-shaped ion conduction pore. Pillared by the four TM1 helices, the transmembrane helices of NfMCU enclose a cone-shaped ion conduction pore with wider opening at the luminal side (Fig. 16, 17A). Interestingly, the pore forming TM2 helix makes very little contact with the TM1 helix of the same subunit; instead, TM2 interacts extensively with a neighboring TM1 (Fig. 16A). Consequently, there is a wide gap between TM1 and TM2 within each subunit at the luminal half of the membrane, which I expect to be sealed by lipid.

NfMCU lacks the canonical re-entrant pore loop and helix that defines the selectivity filter of tetrameric cation channels; instead, the filter residues constitute the first helical turn of TM2. The conserved acidic residues of the DIME motif, which is $_{369}$DTME$_{372}$ in NfMCU, point toward the central axis and are separated by about one helical turn (Fig. 17). Four D369 residues encircle the cytosolic pore entrance of NfMCU with a diagonal distance of about 8.0 Å between carboxylate oxygen atoms. The side chains of E372 form the narrowest part of the filter with the narrowest opposing carboxylate oxygens measuring about 4.5 Å (Fig. 17B). As NfMCU was maintained in 1mM $CaCl_2$ throughout sample preparation, I also observed a strong electron density at the center of the E372 ring, which was assigned as a Ca^{2+} ion chelated by two opposing E372s in a bidentate manner with ion-ligand distances between 2.2 – 2.5 Å, optimal for Ca^{2+} coordination (Fig. 17C, D). The protein packing around the filter region also provides insights into the evolutionary conservation of several residues within the proximity of the DIME motif.

W368 intercalates between TM2 of each subunit with its indole ring oriented nearly vertically; its phenyl ring forms CH/π interactions with the highly conserved P373 in a stacked-like configuration (Biedermannova, 2008, Zondlo, 2013) while the amino group of the pyrrole ring forms intra- and intermolecular hydrogen bonds with the carboxylate oxygen of E372 (Fig. 17C, D). Replacing W368 or P373 with alanine can both result in a mutant channel that no longer mediates Ca^{2+} uptake (Fig. 17E). Thus, the region constituting the selectivity filter of NfMCU is tightly packed and conformationally rigid.

Beyond the selectivity filter, the pore opens into a large, mainly hydrophobic cavity, which widens toward the base of the ion conduction pathway rather than constrict as seen among canonical tetrameric cation channels (Fig. 17A). Whether gating occurs within the ion conducting pore is unclear and warrants further studies. However, our *in vitro* ^{45}Ca flux assay and bacteria calcium uptake assay seem to suggest that NfMCU functions as a constitutively open channel since the only conditions required to stimulate Ca^{2+} uptake is an electrochemical gradient. Our speculation that the ion conducting subunit does not possess any gating function is also supported by the general consensus that gating in the human MCU uniplex is mediated by the MICU1 and MICU2 accessory proteins rather the channel itself (Mallilankaraman, 2012, Kamer, 2014, Patron, 2014, Liu, 2016a).

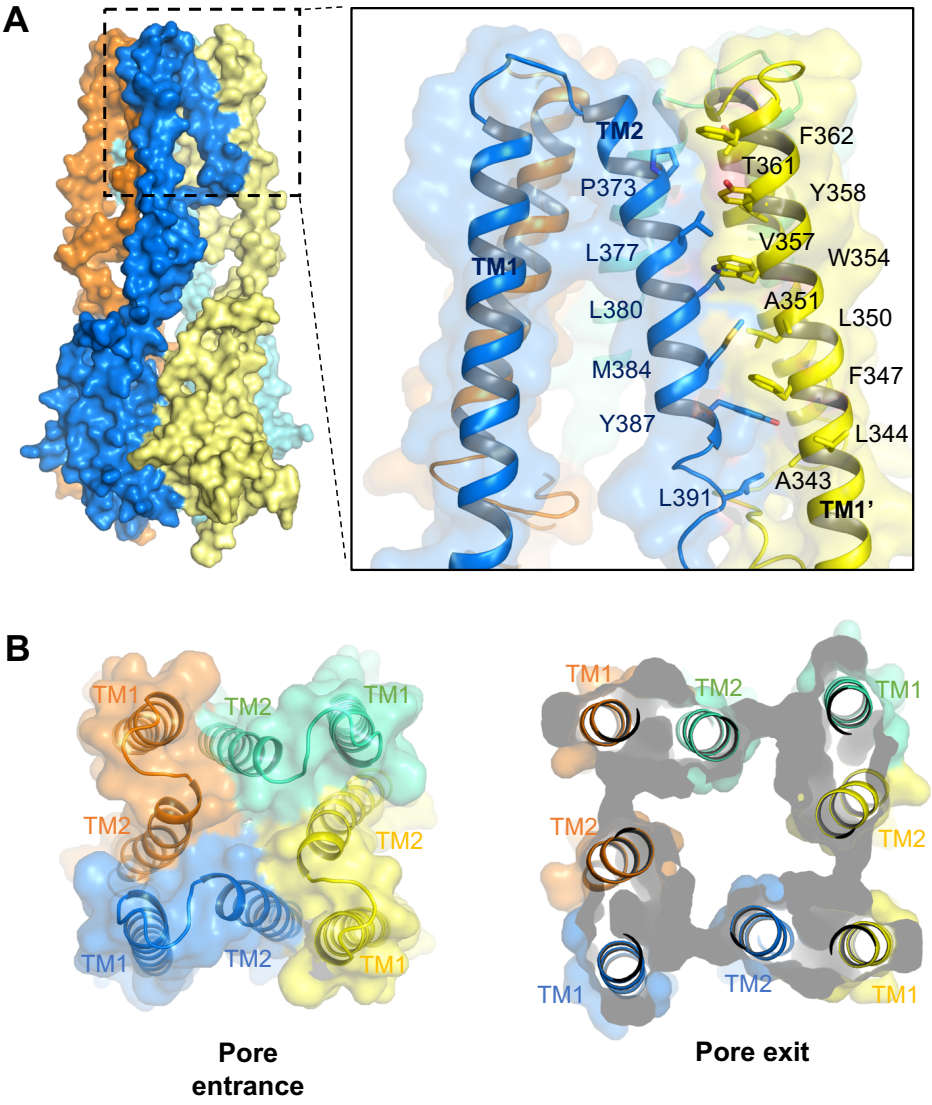

Figure 16. Channel assembly and subunit interfaces at the TMD. A, NfMCU is surface rendered to show intersubunit interactions at the TMD. Inset shows van der Waals interactions between TM2 of one subunit and TM1 of a neighboring subunit. **B**, Top view of NfMCU at the pore entrance and exit, highlighting the unique arrangement of TM helices in channel assembly and the widening of the pore moving down the ion conduction pathway.

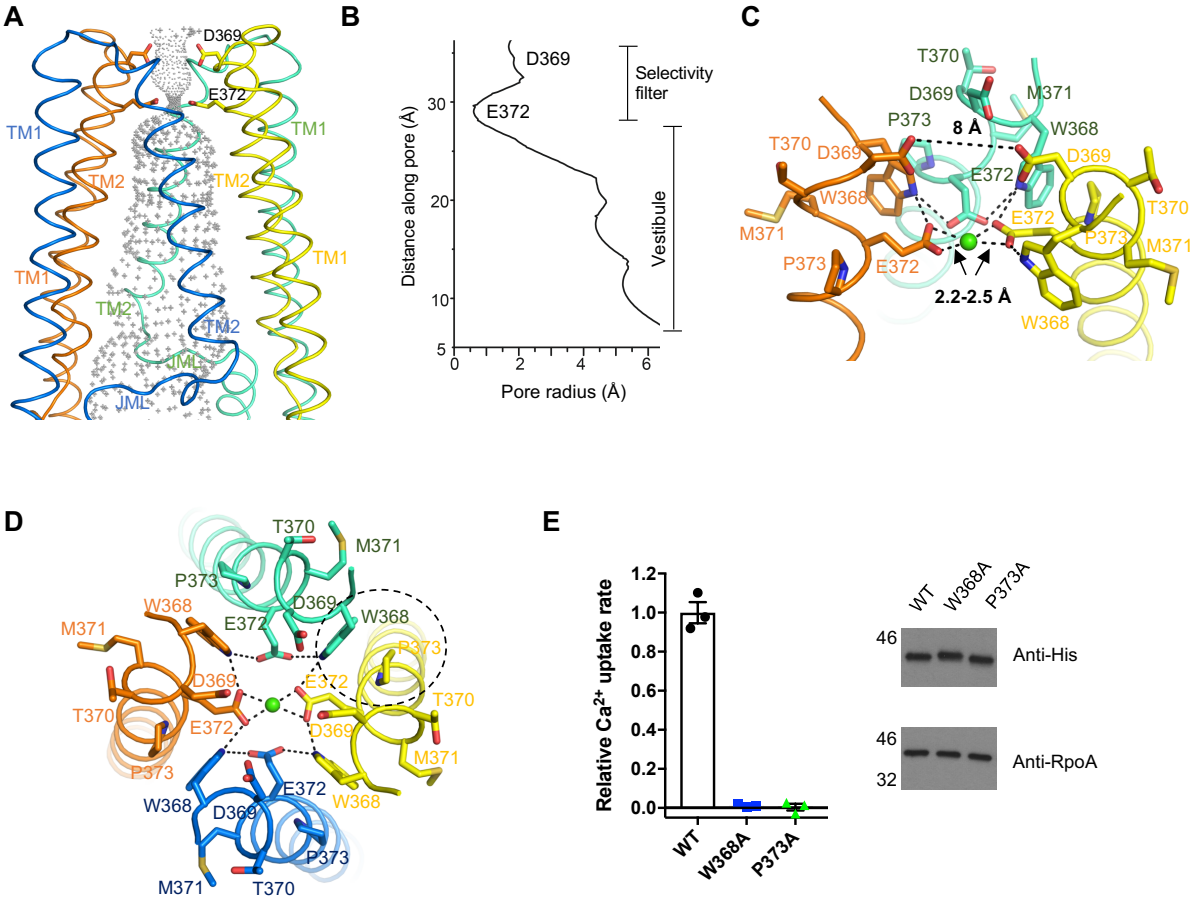
A
D369
E372
TM1
TM1
TM2
TM2
TM1
TM1
TM2
TM2
JML
JML
B
D369
E372
Selectivity filter
Vestibule
Distance along pore (Å)
30
20
10
5
0
2
4
6
Pore radius (Å)
C
T370
D369
M371
P373
8 Å
W368
T370
D369
D369
E372
W368
E372
T370
M371
P373
P373
M371
E372
2.2-2.5 Å
W368
D
T370
M371
P373
W368
D369
W368
M371
E372
P373
D369
E372
T370
T370
E372
D369
M371
P373
E372
W368
W368
D369
P373
M371
T370
E
Relative Ca2+ uptake rate
1.2
1.0
0.8
0.6
0.4
0.2
0.0
WT
W368A
P373A
WT
W368A
P373A
46
Anti-His
46
32
Anti-RpoA

Figure 17. Ion conduction pore of NfMCU. A, Ribbon diagram of the pore domain of NfMCU with the ion conduction pathway rendered as gray mesh and one pair of the acidic filter residues (D369 and E372) shown as sticks. **B**, The radius of the pore was calculated using the program HOLE. E372 forms the narrowest point of the ion conduction pathway, which widens toward the pore exit. **C**, Side view of the selectivity filter, highlighting the arrangement of the DIME motif and the approximate cross distance measurements between D369 residues and Ca^{2+} coordination distances for E372 (shown as dashed lines). The front subunit was removed for visual clarity. **D**, Detailed view of the ion conduction pathway with only TM2s shown. E372 forms an extensive hydrogen bond network with W368. Ca^{2+} is modeled as green sphere, coordinated by a pair of E372 in a bidentate manner. Note the stacked orientation between P373 and the aromatic ring of W368 at the TMD subunit interface (indicated by dashed circle). **E**, Functional activity of NfMCU W368 and P373 mutants expressed in *E. coli*. Cell lysates were analyzed by immunoblotting using anti-His antibody to detect expression of NfMCU. *E. coli* RNA polymerase alpha (RpoA) was used as loading control.

Discussion

In this study, I determined the first full-length structure of the ion conducting subunit (MCU) of the uniplex to near atomic resolution using cryo-EM. Although structure determination of membrane proteins to near atomic resolution or better by cryo-EM have become routine in recent years, there have been very few examples of proteins smaller

than 200kD determined to high resolution. This is due to the inherently low contrast of small protein in vitreous ice. NfMCU, whose total molecular weight as a tetrameric channel is ~180kD, posed a significant technical challenge to structure determination by cryo-EM. Its small size also led me to aggressively pursue its structure by X-ray crystallography. In retrospect, I suspect that NfMCU never crystallized because it is an inherently flexible protein. As shown in Figure 7, NfMCU exhibits a great deal of conformational heterogeneity, which was exacerbated in the NfMCU-Fab complex (Fig. 7B). Additional evidence of conformational heterogeneity is shown in the focused classification of the transmembrane domain (TMD) of the cryo-EM structure of NfMCU. Although I was able to determine the overall structure of NfMCU to 3.8 Å, the TMD was poorly resolved. Approximately one-third of the total particles used for 3D construction of the initial 3.8 Å resolution structure had to be removed to resolve the electron density within the TMD.

The structure of NfMCU also offers clues as to why the channel may be inherently flexible. First, the region located between the coiled-coil domain (CCD) and TMD is highly flexible, as electron density in this region is among the least well-resolved in the overall structure (Fig. 9D, 10D, 15). Second, the gap created between TM1 and TM2 within each subunit, as a result of the protein packing at the TMD, suggests that this region may depend on hydrophobic interactions with lipids to maintain structural stability (Fig. 16A). A consequence of this interaction is that detergent extraction of the protein from the lipid bilayer may disrupt important protein-lipid interactions that could potentially destabilize the purified channel, thus preventing it from crystallizing or alter its function. The unusually wide gap between TM1 and TM2 of NfMCU may also hint at a potential role for the

metazoan-specific, regulatory protein EMRE – to stabilize the TMD of MCU. It has been shown that the both the N- and C-termini of EMRE can be deleted without affecting calcium uptake in human MCU; however, disrupting the interactions between the TMD of MCU and EMRE abolishes mitochondrial calcium uptake (Tsai, 2016). Thus, one possible function of EMRE is to increase the stability of the TMD of MCU by contributing additional protein interactions to MCU. Nonetheless, this does not explain why metazoan MCU, in the absence of EMRE, is nonfunctional. Thus, structural information of the MCU-EMRE complex will hopefully shed new insight into this conundrum.

Additionally, I show that MCU is tetrameric rather than pentameric as reported by the NMR structure of the pore domain of *C. elegans* MCU (cMCU-ΔNTD). Given the controversy in the oligomeric states between NfMCU and cMCU-ΔNTD, I showed that the heterologously expressed NfMCU forms functional channels in *E. coli* (Fig. 5A-D) and that the detergent purified protein remains functional when reconstituted into artificial lipid (Fig. 5E-F). On the other hand, no functional reconstitution was performed on the purified cMCU-ΔNTD in the NMR study. Thus, it is unclear whether the purified cMCU-ΔNTD truly represents a functional channel. A major strength of our study is that NfMCU was reconstituted into artificial lipid discs for structural studies, which should closely mimic the proteoliposomes used in the radioactive calcium flux assay. Thus, our data strongly show that the structure of NfMCU represents that of a functional channel.

Additionally, I determined the crystal structure of the NTD of an algal ortholog of human MCU and show that it adopts a completely different fold than its human counterpart. Although sequence analysis shows that the NTD is poorly conserved among MCU orthologs (Bick, 2012), it is not clear whether the NTD is structurally different. Our

studies, in fact, highlight the difficulty of using computation tools to predict the structures of MCU. The NTD of CrMCU consists of a 3-helical bundle capped by three β-strands while the NTD of NfMCU resembles that of human MCU and consists of a barrel enclosed by a 7-stranded β sheet and an α-helix with a second α-helix capping the barrel. Despite the low sequence similarity among the three MCU orthologs, the NTD of human MCU is surprisingly similar to that of fungal MCU yet completely different from its algal counterpart. While the functional relevance of the NTD of MCU is under debate, it does beg the question as to why MCU has evolved different structures in the NTD but not its pore domain.

Based on the structure of NfMCU, I suspect that the NTD contributes to the tetrameric assembly of MCU by functioning as a scaffolding domain to stabilize the channel in its open, conductive state. Structural comparison between the pore domain of NfMCU and cMCU-ΔNTD shows two contrasting ion conduction pathways. In cMCU-ΔNTD, the region following the selectivity filter is a narrow, elongated cavity with fenestrations near the juxtamembrane helices predicted to be points of exit for ions moving through the channel (Oxenoid, 2016). The narrow ion conduction pathway is maintained by the tight association of the TM2 helices in the pore and the coiled-coil 2 in the luminal, soluble domain of cMCU-ΔNTD (Fig. 14A). On the contrary, the region following the selectivity filter in NfMCU is an open vestibule that widens toward the luminal (or mitochondrial matrix) side of the channel. This open architecture in NfMCU is maintained by coiled-coil 1 and TM1, which form a contiguous α-helix that is anchored on the N-terminal end to the NTD. Thus, absent of the NTD, the coiled-coil domain would likely collapse toward the central axis to form a constricted pore architecture observed in

cMCU-ΔNTD. Although I suspect that the NTD plays a role in maintaining the architectural integrity of the channel, it is not entirely clear whether this domain is essential to the channel's function in cells (Oxenoid, 2016, Lee, 2015). Moreover, the experimental conditions by which the protein was expressed and purified in the NMR study of *C. elegans* MCU pore suggests that the structure of cMCU-ΔNTD is potentially an artifact. Thus, structural comparison between NfMCU and cMCU-ΔNTD warrants caution. Consequently, even absent of the NTD, the ion conduction pathway may not even adopt such a constricted architecture as cMCU-ΔNTD and that ion transport could still occur as reported in the NMR study (Oxenoid, 2016). However, it would be worthwhile to probe this question further using electrophysiology and *in vivo* studies. For instance, does the absence of the NTD perhaps affect single channel behavior such as its conductance or open probability? Additionally, might the NTD serve a functional role *in vivo* that is coupled to mitochondrial calcium uptake? On the contrary, if the NTD does in fact play an insignificant role, why has MCU from different orthologs evolved different folds for this domain over time?

Chapter 4. Mechanism of ion transport and inhibitor binding

Introduction

A central question to the study of ion channels is its mechanism of selectivity. In other words, how do ion channels select for the ions that they transport? Given the tetrameric oligomerization of MCU, the discussion on ion selectivity in this chapter is restricted to that of other tetrameric cation channels such as the 2-TM prokaryotic channels KcsA and NaK, voltage-gated ion channels (VGIC), and transient receptor potential (TRP) channels.

Present in excitable neurons, VGICs belong to the superfamily of tetrameric cation channels and are highly selective for the ions that they conduct (Hille, 1978). Together, they orchestrate the most fundamental function of a neuron – the firing of action potentials, which allow for rapid communication among electrically excitable cells. Among tetrameric cation channels, the ion conducting pore domain adopts a fold that consists of two transmembrane helices connected by a pore helix and a loop – as defined by the prototypical potassium channel KcsA (Fig. 18B) (Doyle, 1998). Although tetrameric cation channels can have additional regulatory domains such as a voltage sensing domain (i.e. voltage-gated ion channels), ligand binding domain (i.e. cyclic nucleotide-gated channels and BK channels), and even an enzymatic domain (i.e. the chanzyme TRPM7) (Krapivinsky, 2014, Yu, 2004), the pore domain constitute the minimal structural element for ion conduction (Fig. 18A). Compared to other tetrameric cation channels, potassium channels are the most well-characterized due to the abundance of functional and structural data in the literature; consequently, they represent the foundation of our

mechanistic understanding of selectivity, which in tetrameric cation channels, is achieved by a stretch of amino acids within the ion conduction pore called the selectivity filter.

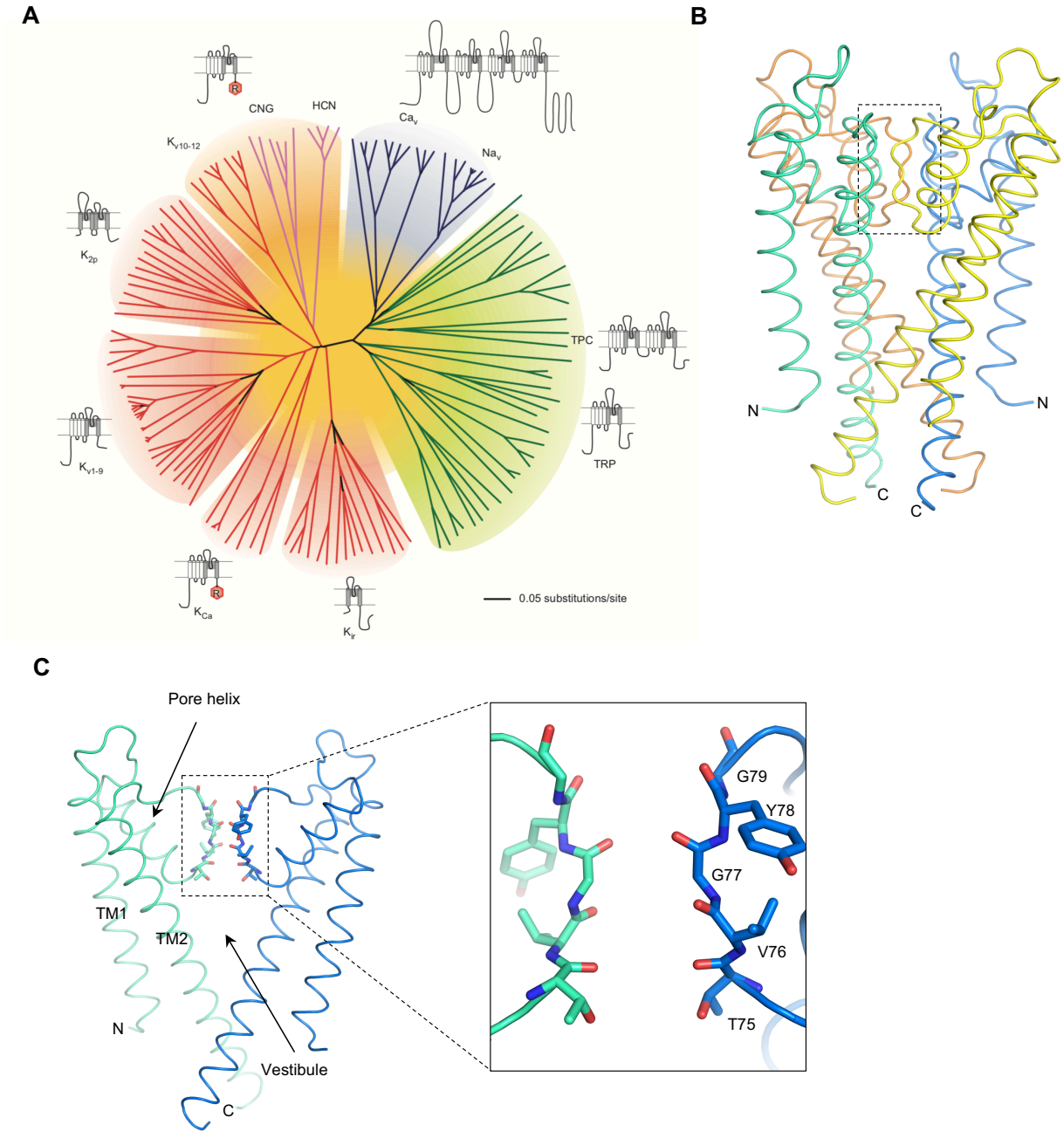

Figure 18. Structural organization of tetrameric cation channels. A, Evolutionary tree of the superfamily of tetrameric cation channels highlighting the structural organization within each family. **B**, Crystal structure of the prototypical potassium channel KcsA (PDB: 1K4D) is shown in ribbon. Each subunit within the tetrameric channel is individually colored. Amino- and carboxy-termini are labeled N and C, respectively. Dashed box highlight the selectivity filter. **C**, Detailed view of KcsA. The front and back subunits are removed for clarity. Inset shows a zoomed-in view of the selectivity filter. Backbone carbonyl oxygens of the TVGYG motif point toward the central axis to coordinate ions.

Potassium selectivity

In potassium channels, the selectivity filter consists of a series of highly conserved amino acids called the TVGYG motif, which confers upon these channels the ability to select for K^+ over Na^+ by a ratio of ~1000:1 (Fig. 18B, C). Early crystal structures of the prokaryotic potassium channel KcsA reveals a selectivity filter that is highly ordered and wide enough to allow the passage of only dehydrated ions. Backbone carbonyl oxygens and the threonine hydroxyl oxygen of the TVGYG motif line the ion conduction pathway to create four square antiprisms, which functions by mimicking the water of hydration to compensate for the energetic cost of dehydration that must occur when ions enter the channel's narrow selectivity filter (Fig. 18C) (Zhou, 2001). Thus, early structural studies on KcsA seem to support a "snug-fit" model to explain how K channels can select for K^+

over Na^+ by a ratio of ~1000:1. Under this model, the selectivity filter is thought to be a rigid scaffold, providing the optimal ligand coordination distance for a dehydrated K^+ but not Na^+, whose hydrated atomic radius is 0.38 Å smaller than K^+.

However, several lines of evidence argue against this model. First, it is understood that proteins are dynamic in solution, capable of sampling an energy landscape that range from fast thermal fluctuations to slow conformational changes (Zaccai, 2000). Thus, it is believed that a 0.38 Å difference between the coordination of K^+ versus Na^+ is sufficiently small enough to be accounted for by thermal fluctuations within the selectivity filter of the channel. This assumption has been supported by molecular dynamics (MD) simulations showing that, indeed, the selectivity filter of KcsA can undergo conformational change ranging from 0.5-1.0 Å during ion conduction and that electrostatic repulsion between carbonyl oxygens within the selectivity filter contributes to K^+ selectivity over Na^+ (Noskov, 2004). Other MD studies have found that the hydration number (the number of water coordinating an ion in solution) and low dielectric property of the selectivity filter are factors that contribute to potassium selectivity (Dudev, 2009). With a preferred hydration number of 7 or 8, K^+ is better coordinated within the square antiprism architecture of a potassium channel selectivity filter than a Na^+, whose optimal hydration number is 6.

In recent years, structural and electrophysiological studies on the non-selective NaK channel from the archaebacterium *Bacillus cereus* and its mutants have shown that the number of contiguous ion-binding sites within the selectivity filter is yet another crucial determinant of K^+ selectivity. It has been shown that the selectivity filter of potassium selective channels possesses four consecutive ion-binding sites while non-selective channels possess two to three binding sites, (Derebe, 2011, Sauer, 2011). With a four-

sited filter, K channels possess two high-affinity K^+ binding sites, which function as a double barrier for blocking Na^+ conductance. This model hypothesizes that, with two high-affinity potassium binding sites, when a K^+ enters the selectivity filter, it is able to equilibrate between the two high-affinity sites, thus blocking Na^+ conduction, until a second K^+ binds to the filter and drives ion conduction as a result of electrostatic repulsion between adjacent ions. On the contrary, with a two- or three-sited filter, a channel possesses only one high-affinity K^+ binding site and binding of Na^+ to a lower affinity site is sufficient to repel the bound K^+ ion and drive ion conduction. Although the debate on the mechanism of potassium selectivity continues, there seems to be a general consensus around the idea that, in addition to the previously described factors, selective potassium permeation occurs by a multi-ion mechanism (Roux, 2017).

Sodium and calcium selectivity

While a great deal is known about potassium selectivity, the mechanism of sodium and calcium selectivity are poorly understood due to the limited structural information about these sodium and calcium channels. Although it is unclear whether the principles of potassium selectivity can be applied to the description of sodium and calcium selectivity, several lines of evidence suggest that the mechanisms are quite different. Unlike, potassium channels, whose selectivity filter is four-fold symmetric, voltage-gated sodium (Na_V) and calcium (Ca_V) channels are believed to possess an asymmetric selectivity filter, which results from a difference in their topology (Tsien, 1987). Potassium channels assemble as four polypeptide chains of a 6-transmembrane (6TM) domain whereas Na_V

and Ca_V channels contain four repeats of a 6TM domain within a single polypeptide chain (Fig. 18A). In Na_V and Ca_V channels, mutational analysis of their selectivity filter sequence shows an unequal contribution of filter residues to ion selectivity (Heinemann, 1992, Yang, 1993). Unlike potassium channels, which utilize their backbone carbonyl oxygens to coordinate ions, Na_V and Ca_V channels utilize their sidechain carboxylate oxygens. In Na_V channels, the DEKA motif constitute the sodium binding site while in Ca_V channels, the EEEE locus constitute the high affinity Ca^{2+} binding site (Heinemann, 1992). Third, Na_V and Ca_V channels have wider pores than K channels; thus, Na^+ and Ca^{2+} are believed to be hydrated or partially hydrated as they move through the pore (Hille, 1975, Tsien, 1987). Fourth, it is believed that Na_V channels possess a single ion binding site within its selectivity filter (Hille, 1975) while Ca_V channels are believed to possess at least two ion binding sites (Hess, 1984).

In recent years, several structures of Na_V and Ca_V channels have been determined, shedding new insights into the mechanism of sodium and calcium selectivity (Payandeh, 2011, Tang, 2014, Wu, 2016, Shen, 2017). While structural studies on prokaryotic Na_V channels and the calcium-selective Ca_VAb channel (a mutant of Na_VAb) have provided atomic resolution views of ion binding in a sodium- and calcium-selective channel, respectively, they may not faithfully reflect the pore architecture and ion coordination of their eukaryotic counterparts. For instance, eukaryotic Na_V channels are believed to possess a single Na^+ binding site within their selectivity filter, which is defined by the DEKA motif, with each residue of the motif positioned on a different 6TM repeat (Hille, 1975). Because prokaryotic Na_V channels assemble as a homotetramer of a 6TM repeat, their pore architecture is four-fold symmetric and their ion coordination lacks the

asymmetry of eukaryotic Na_V channels. Thus, prokaryotic Na_V channels are believed to be more architecturally related to eukaryotic Ca_V channels than their Na_V counterpart. Likewise, in addition to the absence of pore asymmetry in Ca_VAb, its selectivity filter is quite different from eukaryotic Ca_V. To become calcium-selective, three residues in the selectivity filter of Na_VAb had to be mutated to an aspartate ($_{175}$TLESWSM$_{181}$ to $_{175}$TLDDWSD$_{181}$), resulting in a clustering of 12 aspartate residues along the length of the ion conduction pathway. On the contrary, eukaryotic Ca_V channels are calcium selective, whose selectivity filter is defined by an EEEE motif, with each glutamate positioned on a different 6TM repeat within a single polypeptide chain. Moreover, eukaryotic Na_V can be made calcium selective by mutating the alanine and lysine of the DEKA motif to glutamate, thus confirming the relevance of the asymmetric filter sequence in Na_V channels to sodium selectivity (Heinemann, 1992).

Even though only a single ion binding locus has been identified in eukaryotic Na_V and Ca_V channels, functional studies using electrophysiology suggests a multi-ion mechanism of Ca^{2+} permeation for Ca_V channels (Almers, 1984, Hess, 1984). It has been shown that Ca_V channels can conduct Na^+ in the absence of Ca^{2+} in the recording solution. However, micromolar concentrations of Ca^{2+} is sufficient to block the sodium current, which suggests a high-affinity Ca^{2+} binding site (the EEEE locus) that functions to block the permeation of monovalent ions under physiological conditions. On the other hand, >10mM $CaCl_2$ in the recording buffer is needed to achieve half-maximal unitary Ca^{2+} current in Ca_V channels, which suggests a second, lower affinity calcium binding site that functions to allow double occupancy of Ca^{2+} ions to the pore of Ca_V channels to mediate rapid ion conduction (Hess, 1986). The multi-site model of calcium binding is also

supported by the anomalous mole fraction effect observed in Ca_V channels (Hess, 1984, Almers, 1984). Briefly, it was shown that when bathed in a mixed solution of $BaCl_2$ and $CaCl_2$, Ca_V channels exhibit lower conductance than when they are bathed in an equimolar concentration solution of either $BaCl_2$ or $CaCl_2$ alone. In other words, the anomalous mole-fraction effect arises because Ca_V channels have a high affinity site for Ca^{2+} that blocks and repel Ba^{2+} until the concentration of Ca^{2+} is low enough for the channel to conduct Ba^{2+} and vice versa. It is worth noting that the anomalous mole fraction effect was initially observed in potassium channels, allowing for the proposal that the selectivity filter of potassium channels contains four ion-binding sites – an idea proposed a decade prior to the structure determination of the first ion channel (Neyton, 1988). Thus, one possible commonality between potassium and calcium channels is their use of a multi-ion pore for rapid ion conduction, with a high affinity ion binding site that functions to block competing ions in the cellular milieu. However, as previously discussed, potassium channels have two high-affinity K^+ binding sites while Ca_V channels are known to have only one high-affinity Ca^{2+} binding site. Although near atomic resolution (3.6 – 3.8 Å) cryo-EM structures of eukaryotic Na_V and Ca_V channels have been determined recently, electron densities within their selectivity filter are of insufficient quality to pinpoint accurately how ions are coordinated (Wu, 2016, Shen, 2017). Thus, it remains to be seen how ion selectivity is achieved within eukaryotic Na_V and Ca_V channels.

Perhaps the best clue that we currently have for understanding calcium selectivity comes from the crystal structure of the rat transient receptor potential channel TRPV6 (Saotome, 2016). At 3.25 Å resolution, the selectivity filter is well resolved and the identification of bound Ca^{2+} within the protein was confirmed by anomalous diffraction

data. The structure of TRPV6 shows three in-line calcium binding sites with Ca^{2+} coordinated by both side chain carboxylate oxygens (the high-affinity site) and backbone carbonyl and hydroxyl oxygen atoms (the low affinity sites). The high-affinity (site 1) Ca^{2+} binding site is positioned at the luminal mouth of the selectivity filter and consists of four aspartate side chains (D541) directly coordinating a dehydrated Ca^{2+} through their carboxylate oxygens. On the other hand, the two low-affinity binding sites, which consist of main chain carbonyl oxygens and the hydroxyl oxygens of a filter threonine (T538), likely interact with hydrated Ca^{2+} ions through hydrogen bonding. Thus, calcium selectivity is hypothesized to be mediated by the ring of aspartate at site 1, which is expected to be constitutively bound to Ca^{2+} because of the proximity of the D541 side chains. This, in effect, allows the channel to block the permeation of monovalent ions, thus achieving calcium selectivity. Calcium permeation was proposed to follow a “knock-off” mechanism, whereby an elevation in extracellular Ca^{2+} concentration would displace the bound Ca^{2+} at site 1. How this could be achieved is not clear given that extracellular calcium concentrations are already in the millimolar range. Interestingly, the structure of TRPV6 shows a cluster of four acidic residues on each subunit oriented above the mouth of the pore, which is hypothesized to be recruitment sites for Ca^{2+}. These recruitment sites could in essence concentrate Ca^{2+} at the extracellular vestibule to help mediate rapid ion conduction.

MCU and calcium selectivity

The selectivity filter of MCU is structurally distinct from those belonging to the superfamily of tetrameric cation channels (Fig. 17A, 18B). In place of a pore loop, the selectivity filter of MCU constitutes the first helical turn of its TM2 helix, with the side chains of acidic residues from the DIME motif oriented toward the central axis of the ion conduction pathway (Fig. 11B, 17A, C). The proximity of the two rings of acidic residues – D369s and E372s – within the selectivity filter of NfMCU suggests a two-sited single file pore for selective Ca^{2+} permeation in MCU, which is conceptually similar to the classical ion conduction model for voltage-gated Ca^{2+} channel (Almers, 1984, Hess, 1984). With a larger diameter, the ring of D369s at the cytosolic entrance encircles a low affinity Ca^{2+} site (site 1) for a hydrated ion. The site is likely non-specific, but preferable for Ca^{2+} given the highly negative charge of the ring. The narrow ring consisting of E372s forms the high affinity Ca^{2+} selective site (site 2) with the acidic side chains directly chelating the Ca^{2+} ion. Also, the structural constraint of E372 forces the carboxylate side chains to be within close proximity to each other, thus making an empty site 2 energetically unfavorable due to electrostatic repulsion (Fig. 17C, D). To mitigate this effect, I suspect that site 2 is constitutively bound to Ca^{2+} with high electrostatic affinity, which can be accomplished at physiological condition given that MCU has a very high-affinity for Ca^{2+} ($K_D \leq 2nM$). While 100nM $CaCl_2$ is sufficient to completely block the Na^+ current, millimolar concentrations of $CaCl_2$ is needed to achieve half-maximal current, suggesting the presence of a second low affinity Ca^{2+} binding site in MCU (Kirichok, 2004).

Based on the structure of NfMCU, I hypothesize the following mechanism for Ca^{2+} transport (Fig. 19A), which likely follows the same model proposed for voltage-gated Ca^{2+}

channel: Ca^{2+} is constitutively bound to the high-affinity site 2 under physiological condition and, thus, blocks the permeation of Na^{+} or K^{+}. With increasing cytosolic Ca^{2+} concentration, Ca^{2+} starts to occupy the lower affinity site 1 and, thereby, provide the necessary electrostatic repulsion between sites 1 and 2 to lower the affinity of site 2 Ca^{2+}, allowing it to be readily knocked off from site 2 and move into the water filled vestibule directly below the filter. This Ca^{2+} permeation cycle repeats as the Ca^{2+} from site 1 jumps to site 2 freeing site 1 to bind a new Ca^{2+}. The presence of the low affinity site external to the high affinity site may also explain the inward rectification of Ca^{2+} permeation observed in MCU (Kirichok, 2004).

Results

The two-sited model implies that the high affinity site 2 is the essential one for Ca^{2+} selectivity whereas site 1 is less specific, with low affinity, but necessary for efficient Ca^{2+} permeation. The roles of the acidic residues at both sites for Ca^{2+} permeation were tested in NfMCU using our bacteria uptake assay. I first examined the effect of neutralizing the two acidic residues individually by testing the calcium uptake of the D369N and E372Q mutants. Consistent with observations in human MCU (Baughman, 2011, Oxenoid, 2016), the E372Q mutant no longer conducts Ca^{2+} while the D369N mutant exhibited a slight reduction in Ca^{2+} uptake (Fig. 19B). I also asked whether disrupting the ion coordination distance had any effect on channel function. Interestingly, a D369E mutation showed ~50% greater Ca^{2+} uptake rate compared to the WT while the E372D mutant remained nonfunctional. A similar D261E mutation in human MCU – the equivalent mutation as

D369E for NfMCU – showed a slight reduction in calcium uptake (Oxenoid, 2016). Mutating D369 to threonine or glutamine also yielded nonfunctional channels. These data confirm that the site 2 E372, which is essential for specific Ca^{2+} binding, is highly sensitive to mutations whereas the non-specific site 1 D369 is more tolerable to mutations.

The structure of NfMCU also offers a unique opportunity to probe the mechanism of Ru360 binding. In human MCU, a serine (S259) two residues preceding the DIME motif was initially identified to be important for Ru360 binding (Baughman, 2011); in NfMCU, however, the equivalent position is a glycine. Studies on cMCU-ΔNTD identified the aspartate of the DIME motif as a second key residue for Ru360 binding (Cao, 2017), which I suspect is the primary Ru360 binding site for NfMCU since the DIME motif is conserved across all MCU orthologs. I therefore tested the effects of D369 mutations on Ru360 blocking in NfMCU. Neutralizing the aspartate (D369N) weakened Ru360 blocking while maintaining the charge but reducing the pore diameter at site 1 (D369E) eliminated Ru360 blocking (Fig. 19C, D). This result confirms that site 1 D369 in NfMCU forms the primary blocking site for Ru360, whose binding is dictated by the charge as well as the pore size at site 1. Immunoblot analysis shows that the change in channel is not a result of a dramatic change in the protein expression of the NfMCU mutants (Fig. 19E).

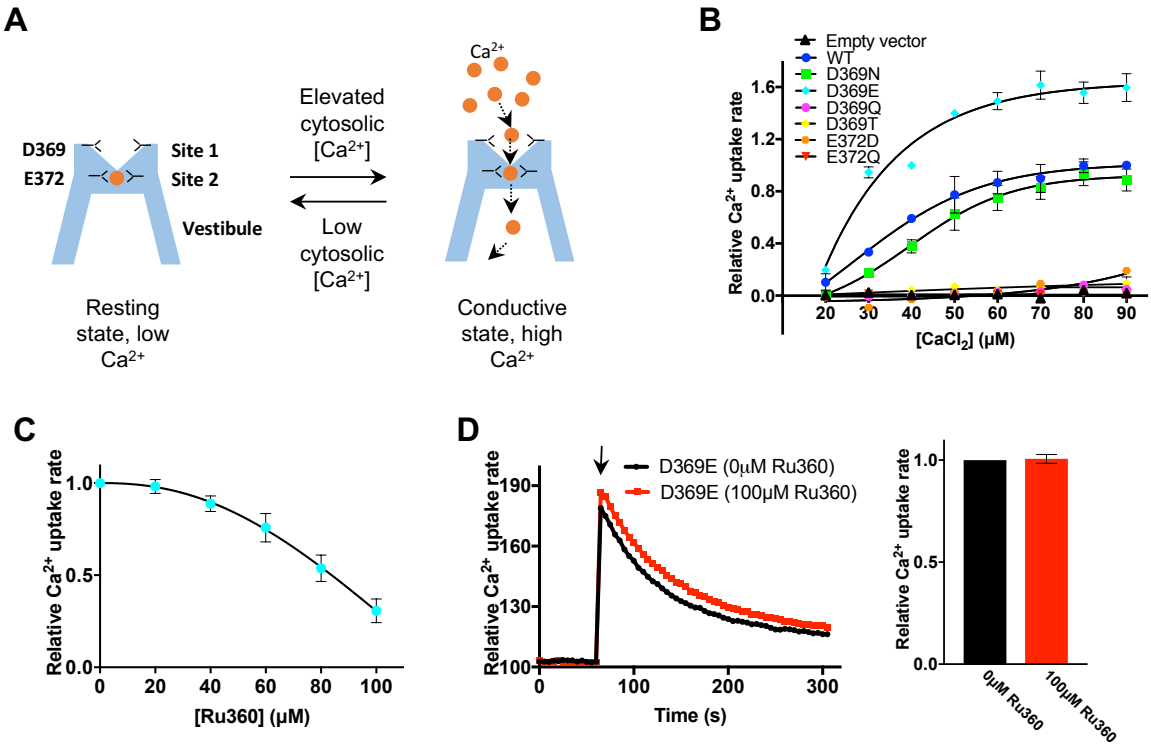
A
D369
E372
Site 1
Site 2
Vestibule
Resting state, low Ca2+
Elevated cytosolic [Ca2+]
Low cytosolic [Ca2+]
Ca2+
Conductive state, high Ca2+
B
Empty vector
WT
D369N
D369E
D369Q
D369T
E372D
E372Q
Relative Ca2+ uptake rate
[CaCl2] (μM)
C
Relative Ca2+ uptake rate
[Ru360] (μM)
D
D369E (0μM Ru360)
D369E (100μM Ru360)
Relative Ca2+ uptake rate
Time (s)
0μM Ru360
100μM Ru360

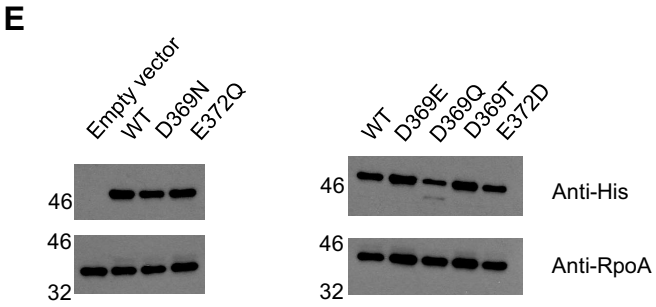
E
Empty vector
WT
D369N
E372Q
WT
D369E
D369Q
D369T
E372D
46
46
32
46
46
32
Anti-His
Anti-RpoA

Figure 19. Mechanism of ion transport and Ru360 inhibition. A, Proposed model of calcium permeation in NfMCU. At rest, Ca^{2+} binds to E372 (site 2) and acts as a permeating blocker to monovalent ions. An increase in cytosolic Ca^{2+} allows binding at D369 (site 1), thus weakening the affinity at site 2, allowing Ca^{2+} to move down the electrochemical gradient and enter the vestibule. The cycle repeats with cytosolic Ca^{2+} pushing from site 1 to site 2 and into the vestibule. **B**, Concentration dependent calcium uptake in E. coli expressing empty vector (black trace) or NfMCU mutants (colored traces). Each point represents rate of calcium uptake normalized to the uptake rate at 90μM $CaCl_2$. Data shown represent mean ± SEM, n=3. **C**, Concentration dependent inhibition of E. coli expressing NfMCU D369N by Ru360. Each point represents rate of calcium uptake normalized to the uptake rate without Ru360 in the reaction. Data shown represent mean ± SEM, n=3. **D**, Representative calcium uptake trace for E. coli expressing NfMCU D369E mutant pulsed with 50μM $CaCl_2$ and 0 μM Ru360 or with 100 μM Ru360. Arrow indicate addition of 50μM $CaCl_2$ to the reaction. Adjacent bar graph shows the rate of calcium uptake normalized to the uptake rate without Ru360 in the reaction; data shown represent mean ± SEM, n=3. **E**, Western blot analysis of NfMCU mutants. Mouse anti-His antibodies (Qiagen) was used to detect NfMCU expression and mouse anti-RpoA targeting *E. coli* RNA polymerase alpha (Santa Cruz Biotechnology) was used for loading control.

Discussion

The structure of NfMCU, thus, provides the first model of an intact mitochondrial calcium uniporter determined to near atomic resolution, shedding new insights into channel assembly and function. Contrary to the structure of cMCU-ΔNTD, NfMCU functions as a tetrameric calcium channel, whose pore is poised for rapid ion conduction. In essence, the channel provides a rather finite barrier measuring about 6 Å – the distance separating the filter aspartate and glutamate – that Ca^{2+} must traverse from the intermembrane space to the mitochondrial matrix. The combination of having two ion binding sites and the presence of a huge electrochemical gradient across the inner mitochondrial membrane provide the necessary driving force for MCU to selectively move Ca^{2+} into the matrix. It is notable that early studies of calcium transport demonstrated that mitochondria from diverse eukaryotes have uniporter activity (Carafoli, 1971). However, in the absence of other uniplex regulatory components, the kinetics and apparent binding affinities of calcium uptake by fungal mitochondria are appreciably different from that of vertebrate mitochondria (Carafoli, 1971). While NfMCU reveals the architectural arrangement of the basic channel component of the uniporter, further study is needed to address some fundamental questions about metazoan uniporter function, such as how metazoan MCU evolved to require EMRE as an essential component for its conduction and how MICU1 and MICU2 confer Ca^{2+}-dependent gating to the uniplex.

References

ADAMS, P. D. E. A. 2010. PHENIX: a comprehensive Python-based system for macromolecular structure solution. Acta Crystallographica D, 66, 213-221.

ALMERS, W., MCCLESKEY, E.W. 1984. Non-selective conductance in calcium channels of frog muscle: calcium selectivity in a single-file pore. J. Physiol. , 353.

AMUNTS, A. E. A. 2014. Structure of the yeast mitochondrial large ribosomal subunit. Science 343, 1485-1489.

BAUGHMAN, J. M., PEROCCHI, F., GIRGIS, H., PLOVANICH, M., BELCHER-TIMME, C.A., SANCAK, Y., BAO, X.R., STRITTMATTER, L., GOLDBERGER, O., BOGORAD, R.L., ET AL. 2011. Integrative genomics identifies MCU as an essential component of the mitochodrial calcium uniporter. Nature 476, 341-45.

BERRIDGE, M. J., BOOTMAN, M.D., RODERICK, H.L. 2003. Calcium signaling: dynamics, homeostasis and remodeling. Nat. Rev. Mol. Cell Biol., 4, 517-29.

BEZPROZVANNY, I., WATRAS, J., EHRLICH, B.E. 1991. Bell-shaped calcium-response curves of Ins(1,4,5)P3- and calcium-gated channels from endoplasmic reticulum of cerebellum. Nature, 351, 751-4.

BICK, A. G., CALVO, S.E., MOOTHA, V.K. 2012. Evolutionary diversity of the mitochondrial calcium uniporter. Science, 336, 886.

BIEDERMANNOVA, L., RILEY, K.E., BERKA, K., HOBZA, P., VONDRASEX, J. 2008. Another role of proline: stabilization interactions in proteins and protein complexes concerning proline and tryptophane. Phys. Chem. Chem. Phys., 10, 6350-59.

BYGRAVE, F. L., RAMACHANDRAN, C., SMITH, R.L. 1977. On the mechanism by which inorganic phosphate stimulates mitochondrial calcium transport. FEBS Lett., 83, 155-8.

CAO, C., WANG, S., CUI, T., SU, X-C., CHOU, J.J. 2017. Ion and inhibitor binding of the double-ring ion selectivity filter of the mitochondrial calcium uniporter. Proc. Natl. Acad. Sci. USA, 114, E2846-E2851.

CARAFOLI, E., LEHNINGER, A.L. 1971. A survey of the interaction of calcium ions with mitochondria from different tissues and species. Biochem. J., 122, 681-90.

CHEN, V. B., ARENDALL, W.B. 3RD, HEADD, J.J., KEEDY, D.A., IMMORMINO, R.M., KAPRAL, G.J., MURRAY, L.W., RICHARDSON, J.S., RICHARDSON, D.C. 2010. MolProbity: all-atom structure validation for macromolecular crystallography. Acta Crystallographica D, 66, 12-21.

CHIURILLO, M. A., LANDER, N., BERTOLINI, M.S., STOREY, M., VERCESI, A.E., DOCAMPO, R. 2017. Different Roles of Mitochondrial Calcium Uniporter Complex Subunits in Growth and Infectivity of Trypanosoma cruzi. MBio, 8, pii: e00574-17.

CLAPHAM, D. E. 2007. Calcium signaling. Cell, 131, 1047-58.

DANEV, R., TEGUNOV, D., BAUMEISTER, W. 2017. Using the Volta phase plate with defocus for cryo-EM single particle analysis. eLife, 6, e23006.

DE BRITO, O. M., SCORRANO, L. 2008. Mitofusin 2 tethers endoplasmic reticulum to mitochondria. Nature, 456, 605-10.

DE STEFANI, D., RAFFAELLO, A., TEARDO, E., SZABO, I., RIZZUTO, R. 2011. A forty-kilodalton protein of the inner membrane is the mitochondrial calcium uniporter. Nature, 476, 336-40.

DELUCA, H. F. A. E., G.W. 1961. Calcium uptake by rat kidney mitochondria. Proc. Natl. Acad. Sci. USA, 47, 1744-50.

DENISOV, I. G., GRINKOVA, Y.V., LAZARIDES, A.A., SLIGAR, S.G. 2004. Directed self-assembly of monodisperse phospholipid bilayer Nanodiscs with controlled size. J. Am. Chem. Soc., 126, 3477-87.

DEREBE, M. G., SAUER, D.B., ZENG, W., ALAM, A., SHI, N., JIANG, Y. 2011. Tuning the ion selectivity of tetrameric cation channels by changing the number of ion binding sites. Proc. Natl. Acad. Sci. USA, 108, 598-602.

DIMAIO, F., ZHANG, J., CHIU, W., BAKER, D. 2013. Cryo-EM model validation using independent map reconstructions. Protein Sci. , 22, 865-868.

DOLMETSCH, R. E., XU, K., LEWIS, R.S. 1998. Calcium oscillations increase the efficiency and specificity of gene expression. Nature, 392, 933-6.

DOYLE, D. A., MORAIS CABRAL, J., PFUETZNER, R.A., KUO, A., GULBIS, J.M., COHEN, S.L., CHAIT, B.T., MACKINNON, R. 1998. The structure of the potassium channel: molecular basis of K+ conduction and selectivity. Science, 280, 69-77.

DUDEV, T., LIM, C. 2009. Determinants of K+ vs Na+ selectivity in potassium channels. J. Am. Chem. Soc., 131, 8092-101.

EMSLEY, P., LOHKAMP, B., SCOTT, W. G. & COWTAN, K. 2010. Features and development of Coot. Acta Crystallographica D, 66, 486-501.

FAN, G., BAKER, M.L., WANG, Z., BAKER, M.R., SINYAGOVSKIY, P.A., CHIU, W., LUDTKE, S.J., SERYSHEVA, I.I. 2015. Gating machinery of InsP3R channels revealed by electron cryomicroscopy. Nature, 527, 336-41.

FOX, N. K., BRENNER, S.E., CHANDONIA, J.M. 2014. SCOPe: Structural Classification of Proteins – extended, integrating SCOP and ASTRAL data and classification of new structures. Nucleic Acids Res., 42, D304-309.

FRAUENFELD, J., LOVING, R., ARMACHE, JP., SONNEN, A.FP., GUETTOU, F., MOBERG, P. ZHU, L., JEGERSCHOLD, C., FLAYHAN, A., BRIGGS, J.A.G., GAROFF, H., LOW, C., CHENG, Y., NORDLUND, P. 2016. A saposin-lipoprotein nanoparticle system for membrane proteins. Nat. Methods 13, 345-51.

GUNTER, T. E., PFEIFFER, D.R. 1990. Mechanisms by which mitochondria transport calcium. Am. J. Physiol. , 258, C755-86.

HEGINBOTHAM, L., KOLMAKOVA-PARTENSKY, L. & MILLER, C. 1998. Functional reconstitution of a prokaryotic K+ channel. J. Gen. Physiol. , 111, 741-749.

HEINEMANN, S. H., TERLAU, H., STÜHMER, W., IMOTO, K., NUMA, S. 1992. Calcium channel characteristics conferred on the sodium channel by single mutations. Nature, 356, 441-3.

HESS, P., LANSMAN, J.B., TSIEN, R.W. 1986. Calcium channel selectivity for divalent and monovalent cations. Voltage and concentration dependence of single channel current in ventricular heart cells. J. Gen. Physiol., 88, 293-319.

HESS, P., TSIEN, R.W. 1984. Mechanism of ion permeation through calcium channels. Nature, 301, 453-56.

HILLE, B. 1975. Ionic selectivity, saturation, and block in sodium channels. A four-barrier model. J. Gen. Physiol., 66, 535-60.

HILLE, B. 2001. Ion Channels of Excitable Membranes, Sunderland, MA, Sinauer Associates, Inc.

HILLE, B., SCHWARZ, W. 1978. Potassium channels as multi-ion single-file pores. J. Gen. Physiol., 72, 409-42.

HOU, X., PEDI, L., DIVER, M.M., LONG, S.B. 2012. Crystal structure of the calcium release-activated calcium channel Orai. Science, 338, 1308-13.

JOUAVILLE, L. S., ICHAS, F., HOLMUHAMEDOV, E.L., CAMACHO, P., LECHLEITER, J.D. 1995. Synchronization of calcium waves by mitochondrial substrates in Xenopus laevis oocytes. Nature, 377, 438-41.

KAMER, K. J., MOOTHA, V.K. 2014. MICU1 and MICU2 play nonredundant roles in the regulation of the mitochondrial calcium uniporter. EMBO Rep. , 15, 299-307.

KAMER, K. J., MOOTHA, V.K. 2015. The molecular era of the mitochondrial calcium uniporter. Nat. Rev. Mol. Cell Biol., 16, 545-53.

KIRICHOK, Y., KRAPIVINSKY, G., CLAPHAM, D.E. 2004. The mitochondrial calcium is a highly selective ion channel. Nature, 427, 360-64.

KOVACS-BOGDAN, E., SANCAK, Y., KAMER, K.J., PLOVANICH, M., JAMBHEKAR, A., HUBER, R.J., MYRE, M.A., BLOWER, M.D., MOOTHA, V.K. 2014. Reconstitution of the mitochondrial calcium uniporter in yeast. Proc. Natl. Acad. Sci. USA, 111, 8985-90.

KRAPIVINSKY, G., KRAPIVINSKY, L., MANASIAN, Y., CLAPHAM, D.E. 2014. The TRPM7 chanzyme is cleaved to release a chromatin-modifying kinase. Cell, 157, 1061-72.

KRISSINEL, E., HENRICK, K. 2004. Secondary-structure matching (SSM), a new tool for fast protein structure alignment in three dimensions. Acta Cryst., 60, 2256-2268

KUCUKELBIR, A., SIGWORTH, F. J. & TAGARE, H. D. 2014. Quantifying the local resolution of cryo-EM density maps. Nat. Methods, 11, 63-65.

LEE, Y., MIN, C.K., KIM, T.G., SONG, H.K., LIM, Y., KIM, D., SHIN, K., KANG, M., KANG, J.Y., YOUN, H-S., ET AL. 2015. Structure and function of the N-terminal domain of the human mitochondrial calcium uniporter. EMBO Rep., 16, 1318-33.

LEHNINGER, A. L., CARAFOLI, E., ROSSI, C.S. 1967. Energy-linked ion movements in mitochondrial systems. Adv. Enzymol. , 29, 259-320.

LIU, J. C., LIU, J., HOLMSTROM, K.M., MENAZZA, S., PARKS, R.J., FERGUSSON, M.M., YU, Z-X., SPRINGER, D.A., HALSEY, C., LIU, C., ET AL. 2016a. MICU1 serves as a molecular gatekeeper to prevent in vivo mitochondrial calcium overload. Cell Rep. , 16, 1561-1573.

LIU, J. C., LIU, J., HOLMSTRÖM, K.M., MENAZZA, S., PARKS, R.J., FERGUSSON, M.M., YU, Z.X., SPRINGER, D.A., HALSEY, C., LIU, C., MURPHY, E., FINKEL, T. 2016b. MICU1 Serves as a Molecular Gatekeeper to Prevent In Vivo Mitochondrial Calcium Overload. Cell Rep., 16, 1561-1573.

LO, C. J., LEAKE, M.C., PILIZOTA, T., BERRY, R.M. 2007. Nonequivalence of membrane voltage and ion-gradient as driving forces for the bacterial flagellar motor at low load. Biophys. J., 93, 294-302.

LOGAN, C. V., SZABADKAI, G., SHARPE, J.A., PARRY, D.A., TORELLI, S., CHILDS, A-M., KRIEK, M., PHADKE, R., JOHNSON, C.A., ROBERTS, N.Y., ET AL. 2014. Loss of function mutations in MICU1 cause a brain and muscle disorder linked to primary alterations in mitochondrial calcium signaling. Nat. Genet., 46, 188-93.

MALLILANKARAMAN, K., DOONAN, P., CARDENAS, C., CHANDRAMOORTHY, H.C., MULLER, M., MILLER, R., HOFFMAN, N.E., GANDHIRAJAN, R.K., MOLGO, J., BIRNBAUM, M.J., ET AL. 2012. MICU1 is an essential gatekeeper for MCU-mediated mitochondrial Ca2+ uptake that regulates cell survival. Cell, 151, 630-644.

MATLIB, M. A., ZHOU, Z., KNIGHT, S., AHMED, S., CHOI, K.M., KRAUSE-BAUER, J., PHILLIPS, R., ALTSCHULD, R., KATSUBE, Y., SPERELAKIS, N., BERS, D.M. 1998. Oxygen-bridged dinuclear ruthenium amine complex specifically inhibits Ca2+ uptake into mitochondria in vitro and in situ in single cardiac myocytes. J. Biol. Chem., 273, 10223-31.

MURPHY, E., PAN, X., NGUYEN, T., LIU, J., HOLMSTRÖM, K.M., FINKEL, T. 2014. Unresolved questions from the analysis of mice lacking MCU expression. Biochem. Biophys. Res. Commun., 449, 384-5.

NEYTON, J., MILLER, C. 1988. Discrete Ba2+ block as a probe of ion occupancy and pore structure in the high-conductance Ca2+ -activated K+ channel. J. Gen. Physiol., 92, 569-86.

NOSKOV, S. Y., BERNÈCHE, S., ROUX, B. 2004. Control of ion selectivity in potassium channels by electrostatic and dynamic properties of carbonyl ligands. Nature, 431, 830-4.

OTWINOWSKI, Z., MINOR, W. 1997. Processing of X--ray diffraction data collected in oscillation mode. Methods Enzymol., 276, 307-26.

OXENOID, K. D., Y., CAO, C., CUI, T., SANCAK, Y., MARKHARD, A., GRABAREK, Z., KONG, L., LIU, Z., OUYANG, B., ET AL. 2016. Architecture of the mitochondrial calcium uniporter. Nature, 533, 269-73.

PAN, X., LIU, J., NGUYEN, T., LIU, C., SUN, J., TENG, Y., FERGUSSON, M.M., ROVIRA, I.I., ALLEN, M., SPRINGER, D.A., APONTE, A.M., GUCEK, M., BALABAN, R.S., MURPHY, E., FINKEL, T. 2013. The physiological role of mitochondrial calcium revealed by mice lacking the mitochondrial calcium uniporter. Nat. Cell Biol., 15, 1464-72.

PATRON, M., CHECCHETTO, V., RAFFAELLO, A., TEARDO, E., REANE, D.V., MANTOAN, M., GRANATIERO, V., SZABO, I., DE STEFANI, D., RIZZUTO, R. 2014. MICU1 and MICU2 finely tune the mitochondrial Ca2+ uniporter by exerting opposite effects on MCU activity. Mol. Cell, 53, 726-37.

PAYANDEH, J., SCHEUER, T., ZHENG, N., CATTERALL, W.A. 2011. The crystal structure of a voltage-gated sodium channel. Nature, 475, 353-8.

PEROCCHI, F., GOHIL, V.M., GIRGIS, H.S., BAO, X.R., MCCOMBS, J.E., PALMER, A.E., MOOTHA, V.K. 2010. MICU1 encodes a mitochondrial EF hand protein required for Ca(2+) uptake. Nature, 467, 291-6.

PETTERSEN, E. F., GODDARD, T.D., HUANG, C.C., COUCH, G.S., GREENBLATT, D.M., MENG, E.C., AND FERRIN, T.E. 2005. UCSF Chimera–a visualization system for exploratory research and analysis. J. Comput. Chem. , 25, 1605–1612.

PLOVANICH, M., BOGORAD, R.L., SANCAK, Y., KAMER., K.J., STRITTMATTER, L., LI, A.A., GIRGIS, H.S., KUCHIMANCHI, S., DE GROOT, J., SPECINER, L., ET AL. 2013. MICU2, a paralog of MICU1, resides within the mitochondrial uniporter complex to regulate calcium handling. PLoS One, 8, e55785.

RAFFAELLO, A., DE STEFANI, D., SABBADIN, D., TEARDO, E., MERLI, G., PICARD, A., CHECCHETTO, V., MORO, S., SZABÒ, I., RIZZUTO, R. 2013. The mitochondrial calcium uniporter is a multimer that can include a dominant-negative pore-forming subunit. EMBO J., 32, 2362-76.

RIZZUTO, R., BRINI, M., MURGIA, M., POZZAN, T. 1993. Microdomains with high Ca2+ close to IP3-sensitive channels that are sensed by neighboring mitochondria. Science, 262, 744-7.

RIZZUTO, R., DE STEFANI, D., RAFFAELLO, A., MAMMUCARI, C. 2012. Mitochondria as sensors and regulators of calcium signalling. Nat. Rev. Mol. Cell Biol., 13, 566-78.

RIZZUTO, R., PINTON, P., CARRINGTON, W., FAY, F.S., FOGARTY, K.E., LIFSHITZ, L.M., TUFT, R.A., POZZAN, T. 1998. Close contacts with the endoplasmic reticulum as determinants of mitochondrial Ca2+ responses. Science, 280, 1763-6.

ROUX, B. 2017. Ion channels and ion selectivity. Essays Biochem., 61, 201-9.

RUSSI, S., JUERS, D.H., SANCHEZ-WEATHERBY, J., PELLEGRINI, E., MOSSOU, E., FORSYTH, V.T., HUET, J., GOBBO, A., FELISAZ, F., MOYA, R., MCSWEENEY, S.M., CUSACK, S., CIPRIANI, F., BOWLER, M.W. 2011. Inducing phase changes in crystals of macromolecules: status and perspectives for controlled crystal dehydration. J. Struct. Biol., 175, 236-43.

SANCAK, Y., MARKHARD, A., KITAMI, T., KOVACS-BOGDAN, E., KAMER, K.J., UDESHI, N.D., CARR, S.A., CHAUDHURI, D., CLAPHAM, D.E., LI, A.A., CALVO, S.E., GOLDBERGER, O., MOOTHA, V.K. 2013. EMRE is an essential component of the mitochondrial calcium uniporter. Science, 342, 1379-82.

SAOTOME, K., SINGH, A.K., YELSHANSKAYA, M.V., SOBOLEVSKY, A.I. 2016. Crystal structure of the epithelial calcium channel TRPV6. Nature, 534, 506-11.

SAUER, D. B., ZENG, W., RAGHUNATHAN, S., JIANG, Y. 2011. Protein interactions central to stabilizing the K+ channel selectivity filter in a four-sited configuration for selective K+ permeation. Proc. Natl. Acad. Sci. USA, 108, 16634–39.

SCARPA, A., AZZONE, G.F. 1970. The mechanism of ion translocation in mitochondria. 4. Coupling of K+ efflux with Ca2+ uptake. Eur. J. Biochem., 12, 328-35.

SCHERES, S. H. 2012. RELION: implementation of a Bayesian approach to cryo-EM structure determination. J. Struct. Biol. , 180, 519-530.

SCHRÖDINGER, L. 2015. The PyMOL Molecular Graphics System, Version 1.8.

SHEN, H., ZHOU, Q., PAN, X., LI, Z., WU, J., YAN, N. 2017. Structure of a eukaryotic voltage-gated sodium channel at near-atomic resolution. Science, 355, eaaI4326.

SMART, O. S., NEDUVELIL, J. G., WANG, X., WALLACE, B. A. & SANSOM, M. S. 1996. HOLE: a program for the analysis of the pore dimensions of ion channel structural models. J. Mol. Graph. , 14, 354-360.

SONG, J., LIU, X., ZHAI, P., HUANG, J., LU, L. 2016. A putative mitochondrial calcium uniporter in A. fumigatus contributes to mitochondrial Ca2+ homeostasis and stress responses. Fungal Genet. Biol. , 94, 15-22.

SZABADKAI, G., BIANCHI, K., VÁRNAI, P., DE STEFANI, D., WIECKOWSKI, M.R., CAVAGNA, D., NAGY, A.I., BALLA, T., RIZZUTO, R. 2006. Chaperone-mediated coupling of endoplasmic reticulum and mitochondrial Ca2+ channels. J. Cell Biol., 175, 901-11.

TANG, L., GAMAL EL-DIN, T.M., PAYANDEH, J., MARTINEZ, G.Q., HEARD, T.M., SCHEUER, T., ZHENG, N., CATTERALL, W.A. 2014. Structural basis for Ca2+ selectivity of a voltage-gated calcium channel. Nature, 505, 56-61.

TSAI, M.-F., PHILLIPS, C.B., RANAGHAN, M., TSAI, C-W., WU, Y., WILLLIAMS, C., MILLER, C. 2016. Dual functions of a small regulatory subunit in the mitochondrial calcium uniporter complex. eLife, e15545.

TSIEN, R. W., HESS, P., MCCLESKEY, E.W., ROSENBERG, R.L. 1987. Calcium channels: mechanisms of selectivity, permeation, and block. Annu. Rev. Biophys. Biophys. Chem., 16, 265-90.

VASINGTON, F. D., MURPHY, J.V. 1962. Ca++ uptake by rat kidney mitochondria and its dependence on respiration and phosphorylation. J. Biol. Chem., 237, 2670-7.

WALLACE, D. C. 2005. A Mitochondrial Paradigm of Metabolic and Degenerative Diseases, Aging, and Cancer: A Dawn for Evolutionary Medicine. Annu. Rev. Genet., 39, 359-407.

WANG, L., YANG, X., LI, S., WANG, Z., LIU, Y., FENG, J., ZHU, Y., SHEN, Y. 2014. Structural and mechanistic insights into MICU1 regulation of mitochondrial calcium uptake. EMBO J. , 33, 594-604.

WU, G., LI, S., ZONG, G., LIU, X., FEI, S., SHEN, L., GUAN, X., YANG, X., SHEN, Y. 2018. Single channel recording of a mitochondrial calcium uniporter. Biochem. Biophys. Res. Commun.

WU, J., YAN, Z., LI, Z., QIAN, X., LU, S., DONG, M., ZHOU, Q., YAN, N. 2016. Structure of the voltage-gated calcium channel Ca(v)1.1 at 3.6 Å resolution. Nature, 537, 191-196.

WU, J., YAN, Z., LI, Z., YAN, C., LU, S., DONG, M., YAN, N. 2015. Structure of the voltage-gated calcium channel Cav1.1 complex. Science, 350, aad2395.

YAFFE, M. 1991. Analysis of mitochondrial function and assembly. Methods Enzymol. , 194, 627-43.

YAN, Z., BAI, X., YAN, C., WU, J., LI, Z., XIE, T., PENG, W., YIN, C., LI, X., SCHERES, S.H.W., SHI, Y., YAN, N. 2015. Structure of the rabbit ryanodine receptor RyR1 at near-atomic resolution. Nature, 517, 50-55.

YANG, J., ELLINOR, P.T., SATHER, W.A., ZHANG, J.F., TSIEN, R.W. 1993. Molecular determinants of Ca2+ selectivity and ion permeation in L-type Ca2+ channels. Nature, 366, 158-61.

YING, W. L., EMERSON, J., CLARKE, M.J., SANADI, D.R. 1991. Inhibition of mitochondrial calcium ion transport by an oxo-bridged dinuclear ruthenium ammine complex. Biochemistry, 30, 4949-52.

YU, F. H., CATTERALL, W.A. 2004. The VGL-chanome: a protein superfamily specialized for electrical signaling and ionic homeostasis. Sci. STKE, 2004, re15.

ZACCAI, G. 2000. How soft is a protein? A protein dynamics force constant measured by neutron scattering. Science, 288, 1604-7.

ZHANG, K. 2016. Gctf: Real-time CTF determination and correction. J. Struct. Biol. , 193, 1-12.

ZHENG, S. Q., PALOVCAK, E., ARMACHE, J.P., VERBA, K.A., CHENG, Y., AGARD, D.A. 2017. MotionCor2: anisotropic correction of beam-induced motion for improved cryo-electron microscopy. Nat. Methods 14, 331-32.

ZHOU, Y., MORAIS-CABRAL, J.H., KAUFMAN, A., MACKINNON, R. 2001. Chemistry of ion coordination and hydration revealed by a K+ channel-Fab complex at 2.0 A resolution. Nature, 414, 43-8.

ZONDLO, N. J. 2013. Aromatic-proline interactions: electronically tunable CH/ interactions. Acc. Chem. Res., 46, 1039-49.

ZÜCHNER, S., MERSIYANOVA, I.V., MUGLIA, M., BISSAR-TADMOURI, N., ROCHELLE, J., DADALI, E.L., ZAPPIA, M., NELIS, E., PATITUCCI, A., SENDEREK, J., PARMAN, Y., EVGRAFOV, O., JONGHE, P.D., TAKAHASHI, Y., TSUJI, S., PERICAK-VANCE, M.A., QUATTRONE, A., BATTALOGLU, E., POLYAKOV, A.V., TIMMERMAN, V., SCHRÖDER, J.M., VANCE, J.M. 2004. Mutations in the mitochondrial GTPase mitofusin 2 cause Charcot-Marie-Tooth neuropathy type 2A. Nat. Genet., 36, 449-51.